

CSI-EPT

TOWARDS PRACTICAL IMPLEMENTATION

CSI-EPT

TOWARDS PRACTICAL IMPLEMENTATION

Msc. Thesis

by

Jiying DAI

This thesis has been approved by

promotor: dr. R.F. Remis

copromotor: dr. W.M. Brink

Members of Thesis Committee:

Title and name,	Function (in organisation) and Affiliation (section)
Dr. ir. R.F. Remis,	Associate professor, TU Delft, Circuits and Systems
Dr. M. Spirito,	Associate professor, TU Delft, Microelectronics
Dr. ir. C.A.T. van den Berg	UMC Utrecht, Division Imaging
Dr. ir. W.M. Brink,	Postdoctoral researcher, LUMC Leiden, C.J. Gorter Center



Keywords: EPT, CSI-EPT, high-field MRI, wavefield imaging, radiofrequency field
...

Printed by: Jiying Dai

An electronic version of this dissertation is available at
<http://repository.tudelft.nl/>.

CONTENTS

Abstract	vii
1 Introduction	1
1.1 Background	2
1.2 State of the art	2
1.3 Problem statement	3
1.4 Aims and methodology	4
1.5 Notation conventions	4
1.6 Thesis outline	4
References	6
2 Basic Theories	7
2.1 Electromagnetic fields in MRI	8
2.1.1 Polarized radiofrequency field	8
2.1.2 Mathematical conventions	9
2.1.3 Helmholtz equation for magnetic field	9
2.1.4 Integral equations	10
2.2 Contrast Source Inversion method	11
2.2.1 Initial condition	12
2.2.2 Green's tensors	13
References	15
3 General Configuration	17
3.1 Experimental setup	18
3.2 Simulation setup	20
References	23
4 Simulation Studies	25
4.1 Regular CSI-EPT with transmit phase input	26
4.1.1 Channel-wise transmission and reception	26
4.1.2 Quadrature mode for transmission and reception	28
4.2 Regular CSI-EPT implementing Transceive Phase Assumption	29
4.2.1 Channel-wise transmission and reception	30
4.2.2 Quadrature excitation for transmission and anti-quadrature for re- ception.	30
4.3 Transmit Phase Correcting CSI-EPT	32
4.3.1 Performance	33
4.3.2 Robustness.	33
4.4 Summary	36
References	38

5	Experimental Studies	39
5.1	Measured transmit field data evaluation	40
5.1.1	Incident field calibration	40
5.1.2	2D approximation	44
5.2	CSI-EPT with measured transmit field input	45
5.3	Summary	47
6	Conclusion	49
A	Polarization of RF Fields	53
	Acknowledgements	59

ABSTRACT

The information of electrical properties of biological tissues within human body can be useful information for diagnosis, tissue characterization, hyperthermia treatment planning and MR safety control.

CSI-EPT is an MR base imaging modality, which reconstructs the electrical properties of the sample. However, this method have not been implemented in practice due to the following issues

1. The exact transmit phase is not available from acquisition.
2. The incident field cannot be measured directly.
3. The loss of sensitivity at those regions with low electrical fields.
4. The sufficiency of 2D configuration, which has been used in most published results, have not be verified.

This thesis investigates the experimental feasibility of CSI-EPT through simulations and phantom experiments, implementing a parallel transceive array under two different excitation modes. After which we give answers or improvements to the above issues.

1

INTRODUCTION

This chapter introduces the background, motivation, and main challenges of this project, along with the general structure and the conventions that will be used in this thesis.

This thesis studies MR-based Contrast Source Inversion - Electrical Properties Tomography (CSI-EPT) at 7 Tesla, for the goal of bringing the method to practical use. During this project, we explore the gaps between theory and practice by simulations and phantom experiments. Moreover, possible solutions are evaluated. In this chapter, the background is reviewed firstly, then target problems are specified, followed by the aims of this project. At the end of the chapter, an outline of this thesis is given.

1.1. BACKGROUND

ELECTRICAL properties of biological tissues are mostly referred to as electrical permittivity and conductivity, which are very useful information for diagnosis and treatment [1]. Knowledge of electrical properties can help characterize geometry and functions inside human body. For example, ECG (Electrocardiography) and EIT (Electrical Impedance Tomography) are widely used for heart and lung functions monitoring, MIT (Magnetic induction tomography) has applications in brain imaging and cryosurgery monitoring. Moreover, these frequency-dependent properties are essential to studies of electromagnetic field interactions inside human body, which is a topic gaining increasing attention recently. For instance, knowledge of electrical properties is helpful for hyperthermia treatment planning and specific absorption rate (SAR) prediction in MRI.

1.2. STATE OF THE ART

ELECTRICAL Properties tomography (EPT) is an MR-based imaging modality that reconstructs electric permittivity map and conductivity map of targeting region, from measured transmit radio frequency (RF) field (B_1^+). This chapter presents the state of art of EPT, by introducing a few already-published EPT algorithms.

EPT has been introduced from Haacke's formula [2],

$$\kappa = (-\nabla^2 B_1^+) / (\omega^2 \mu_0 B_1^+), \quad (1.1)$$

which is based on the homogeneous Helmholtz equation

$$\kappa^2 \mathbf{B} - \nabla^2 \mathbf{B} = 0. \quad (1.2)$$

which will be explained further in next chapter. The corresponding EPT algorithm assumes the magnetic field to be homogeneous. As a result of this assumption, in those regions with effectively varying magnetic field (may be caused by the variance of the incident field or mostly by the variance of object's electrical properties), distortion occurs due to the loss of homogeneity. Moreover, there have not been any published method that is capable of acquiring pure transmit phase yet. Therefore, when firstly applying EPT experimentally in 2003, Wen *et al.* approximates transmit phase by half of the acquired transceive phase with the implementation of a quadrature birdcage[3], which is the well-known Transceive Phase Assumption (TPA).

Later, Voigt *et al.* proposed an algorithm that quantifies electric conductivity and permittivity respectively from transmit phase and B_1^+ amplitude. This method does not solve the boundary issue, and it depends on TPA. Moreover, to separate the quantification of EPs, another two assumptions are involved in to describe the electrical conduc-

tivity with only B_1^+ amplitude and permittivity with only transmit phase, which is not true in practice.

In 2013, cr-MREPT (Convection-Reaction Equation Based Magnetic Resonance Electrical Properties Tomography) and generalized LMT (Local Maxwell Tomography) were proposed [4][5], both of which are improved at those regions of fast varying electrical properties, by feeding an EP-dependent source to the right-hand side of eq. 1.2, which was zero in homogeneous Helmholtz equation. However, due to a second order derivative of magnetic field, which amplifies the noise significantly, generalized LMT has not achieved the noise tolerance that is qualified in practice. Moreover, the second order derivative also contributes to non-negligible boundary errors. Meanwhile, cr-EPT is reported to have stabilization issues at regions with low convection term [4].

The above EPT algorithms are all based on or evolved from Haacke's formula. As a result, even though a few of them have improved the boundary issue by modifying Helmholtz equation, a second order gradient of magnetic field is involved inherently, resulting in amplification of noise.

CSI-EPT (Contrast Source Inversion Electrical Properties Tomography) originates from a nonlinear inversion method by Peter M. van den Berg and Ralph E. Kleinman[6], and was introduced by Balidemaj *et al.* in 2015 [7]. Different from conventional EPT, CSI-EPT is based on electromagnetic field integral equations, for which reason the reconstruction performance does not rely on the assumption of field homogeneity any more. Moreover, there is no gradient on data in CSI-EPT, which helps avoid amplification of noise. CSI-EPT reconstructs unknown fields and contrasts simultaneously, by iteratively minimizing the discrepancy between measured and reconstructed B_1^+ and the discrepancy in the object equation. Therefore, CSI-EPT should not be bothered by noise amplification issue in principle. Moreover, since electrical fields are also reconstructed in each iteration, it is possible to reconstruct specific absorption rate (SAR) map at the same time, which would allow for direct assessment of RF safety. These advantages motivate us to do further study on CSI-EPT, and to put an effort into bringing this method towards clinical use.

1.3. PROBLEM STATEMENT

IN the following section, we discuss the current gaps between CSI-EPT and practical implementation.

TRANSMIT PHASE UNAVAILABILITY

As aforementioned, experimental measurement of transmit phase has not been shown to date. While CSI-EPT method relies on transmit phase. As a result, like most of the previously proposed EPT algorithms, CSI-EPT depends on Tansceive Phase Assumption (TPA), which is only valid under certain symmetry assumptions.

SENSITIVITY AT LOW E -FIELD REGIONS

In CSI-EPT, the unknown contrast is updated based on the reconstructed electrical fields. As a result, the algorithm is sensitive to those regions with low E -field, where corruptions may occur [7]. For the concern of low E -field issue, it is less flexible when determining the elements for transmission and reception.

CALIBRATION OF INCIDENT FIELD

Since CSI-EPT is based on electromagnetic integral equation, the incident field is also required as input. While the incident field haven't been able to be measured accurately. Therefore, the calibration of measured or estimated incident field is required before reconstruction.

2D APPROXIMATION

Most research results about CSI-EPT have been based on a two-dimensional configuration. However, the sufficiency of 2D configuration on approximating the actual 3D conditions needs to be evaluated.

1.4. AIMS AND METHODOLOGY

THIS project aims on bringing 2D CSI-EPT to clinical use, by investigating above three issues by simulations and phantom experiments study.

- About the first issue, we will evaluate the performance of TPA on a simulated 2D model. We will also introduce a modification of regular CSI-EPT method to adapt it to transceive phase input.
- About the second issue, we will evaluate the performance of different transceive modes using a parallel transceiver array.
- About the third issue, we will learn from the correspondence between the acquired transmit field data and the simulated data. Since the simulated data is based on an estimated incident field, the discrepancy between the measured data and the simulated data should be able to characterize the mismatch of incident fields.
- The last issue will be resolved by the comparison of the resulting transmit fields and their CSI-EPT reconstructions between the 2D model and the simulated 3D model, where perturbations from the practical side would be ruled out.

1.5. NOTATION CONVENTIONS

This following table defines the notation conventions that will be used throughout this thesis.

Font	Meaning
<i>Italic</i>	Variables
Bold	Vectors
Roman in Math	Constants
Blackboard (\mathbb{B})	Special sets
Monospace	Code language (MATLAB)

1.6. THESIS OUTLINE

This part presents an outline of this thesis.

Chapter 2: Basic theories

The principles of conventional EPT and regular 2D CSI-EPT.

Chapter 3: General configuration

The setups of relevant simulations and phantom experiments.

Chapter 4: Simulation studies

Study of the field maps, transceive modes, different CSI-EPT algorithms and implementations based of 2D simulation.

Chapter 5: Experimental studies

Experimental feasibility test of CSI-EPT, by comparison between measurements and simulations, along with the mismatch locating and resolving.

Conclusion**Appendix**

Mathematical descriptions of field polarity modes under different excitation modes.

REFERENCES

- [1] C. Gabriel *et al.*, *The dielectric properties of biological tissues: I. Literature survey*, *Phys. Med. Biol.* **41**, 2231 (1996).
- [2] E. M. Haacke *et al.*, *Extraction of conductivity and permittivity using magnetic resonance imaging*, *Phys. Med. Biol.* **38**, 471 (1991).
- [3] H. Wen, *Noninvasive quantitative mapping of conductivity and dielectric distributions using rf wave propagation effects in high-field MRI*, *Proc. SPIE* **471-477**, 5030 (2003).
- [4] S. Hafalir *et al.*, *Convection-reaction equation based magnetic resonance electrical properties tomography (cr-MREPT)*, *IEEE Transactins on Medical Imaging* **33**, 777 (2014).
- [5] D. K. Sodickson *et al.*, *Generalized local maxwell tomography for mapping of electrical property gradients and tensors*, presented at the 21th Annu.Meet. ISMRM, Salt Lake City, UT (2013).
- [6] P. M. van den Berg and R. E. Kleinman, *A contrast source inversion method*, *Inverse Problems* **13**, 1607 (1997).
- [7] E. Balidemaj *et al.*, *CSI-EPT: A contrast source inversion approach for improved MRI-based electric properties tomography*, *IEEE Transactins on Medical Imaging* **34**, 1788 (2015).

2

BASIC THEORIES

This chapter presents the theory background of this project.

This chapter presents the theory background of this project by introducing fundamental principles and some relevant concepts of conventional EPT and CSI-EPT.

2.1. ELECTROMAGNETIC FIELDS IN MRI

FOR conventional MRI systems, where the strength of static magnetic field B_0 is lower than 0.5 T, the interaction between RF field (B_1) and human body is negligible. But the signal-to-noise ratio (SNR) of low B_0 field is not high enough for some advanced studies (e.g. functional MRI) [1]. For pursuing of improved SNR, high-field MRI has been investigated.

As strength of B_0 increases, the Larmor frequency increases linearly, so does the frequency of B_1 field. This results in stronger interactions between human body and B_1 field. For instance, in a 7-Tesla MR system, the frequency of B_1 field is 300 MHz, with wavelength one meter, which is close to the size of human body, then scattering between radiofrequency waves and human body becomes non-negligible any more. As a result, the homogeneity of B_1 is decreased and associated electrical field arises, which brings in safety concern. But at the same time, the advantage of stronger interactions and higher SNR can be used. EPT is based on such interactions between B_1 field and human body, and high-field MR provides efficiently high SNR for applications of this method.

Therefore, investigations in this project are based on radiofrequency (RF) field. All magnetic fields mentioned in this thesis refer in particular to the B_1 field.

2.1.1. POLARIZED RADIOFREQUENCY FIELD

Specifically, EPT is based on transmit field B_1^+ and receive field B_1^- , which respectively represent the polarized component rotating in the same direction of nuclear precession and the polarized component rotating in the opposite direction of nuclear precession. Their mathematical representation is

$$B_1^+ = \frac{B_{1x} + jB_{1y}}{2}, \quad (2.1a)$$

$$B_1^- = \frac{B_{1x} - jB_{1y}}{2}, \quad (2.1b)$$

where B_{1x} and B_{1y} are x-component and y-component of B_1 field. The x,y-components can be represented with the following equations [2]:

$$B_{1x} = KI_o C_x e^{j(\phi+\alpha)}, \quad (2.2a)$$

$$B_{1y} = KI_o C_y e^{j(\phi+\beta)}, \quad (2.2b)$$

where K is a scaling factor depending on coil-geometry, I_o and ϕ are amplitude and phase of the input current of coil, C_x and C_y are frequency- and spatial-attenuation factors, α and β are frequency- and spatial-dependent phase delays. The polarization mode of transceive fields depends on the amplitude and phase of x,y-component. When $\alpha - \beta = n\pi$, with $n \in \mathbb{Z}$, rotating B_1 fields are linearly polarized. When $\alpha - \beta = n\pi + \frac{\pi}{2}$, rotating B_1 fields are circularly polarized. From experimental side, A single dipole produces a linearly polarized field in free space; exciting two perpendicular components

with the same amplitude and 90° phase delay generates a circularly polarized field in free space [3]. However, as electrical conductivity increases within the target region, the conductivity-dependent induced currents will also generate a magnetic field, which will interact with the the linearly polarized field. As a result, an elliptically polarized field will be finally observed. The same condition happens to circular polarization.

The acquired phase data is the transceive phase, which is the suppression of B_1^+ phase and B_1^- phase:

$$\phi^\pm = \phi^+ + \phi^-. \quad (2.3)$$

2.1.2. MATHEMATICAL CONVENTIONS

Before introducing the theories, a few important conventions and definitions are shown below.

- In this project, we use the convention $s = j\omega$, where $\omega = 2\pi f$, f is the operating frequency of the MR system.
- The inner product is defined as

$$\langle f, g \rangle_{\mathbb{S}} = \int_{x \in \mathbb{S}} f(\mathbf{r}) \bar{g}(\mathbf{r}) dV, \quad (2.4)$$

where the overline denotes complex conjugate.

- The adjoint operator L^* satisfies:

$$\langle r, LE \rangle = \langle L^* r, E \rangle \quad (2.5)$$

2.1.3. HELMHOLTZ EQUATION FOR MAGNETIC FIELD

Conventional EPT algorithms are typically based on the homogeneous Helmholtz equation or its variants, and assuming the object to have homogeneous magnetic field, equivalently, homogeneous or slowly-varying global magnetic field.

The Helmholtz equation for the magnetic field can be derived from Maxwell equations, and it starts from Ampère's law:

$$\nabla \times \mathbf{B} = \mu_0(\mathbf{J} + j\omega\epsilon\mathbf{E}), \quad (2.6)$$

with $\mathbf{J} = \sigma\mathbf{E}$, it becomes

$$\nabla \times \mathbf{B} = j\omega\mu_0\kappa\mathbf{E}, \quad (2.7)$$

where $\kappa = \epsilon - j\frac{\sigma}{\omega}$ is the complex electrical permittivity, and it includes electrical conductivity and permittivity respectively in its imaginary part and real part. As the main goal of EPT is to map the electrical properties, reconstructing κ from electromagnetic fields is the core mission of EPT algorithms.

To obtain the Helmholtz equation of magnetic field, take the curl of both sides of eq. 2.7:

$$\nabla \times \nabla \times \mathbf{B} = j\omega\mu_0\nabla \times \kappa\mathbf{E}, \quad (2.8)$$

Apply the following calculus identity:

$$\nabla \times \varphi \mathbf{F} = \varphi \nabla \times \mathbf{F} + \nabla \varphi \times \mathbf{F}, \quad (2.9)$$

where φ is a scalar variable and \mathbf{F} is a vector field, we come to

$$\nabla \times \nabla \times \mathbf{B} = j\omega\mu_0(\kappa\nabla \times \mathbf{E} + \nabla\kappa \times \mathbf{E}), \quad (2.10)$$

Then apply Faraday's Law ($\nabla \times \mathbf{E} = -j\omega\mathbf{B}$), leading to the Helmholtz equation,

$$\nabla^2 \mathbf{B} + \mu_0\omega^2 \kappa \mathbf{B} = -\frac{\nabla\kappa}{\kappa} \times (\nabla \times \mathbf{B}). \quad (2.11)$$

If the medium is homogeneous, the right side will be zero, which leads to the homogeneous Helmholtz equation

$$\nabla^2 \mathbf{B} + \mu_0\omega^2 \kappa \mathbf{B} = 0, \quad (2.12)$$

and its variant, Haacke's formula

$$\kappa = -\frac{\nabla^2 B_1^+}{\mu_0\omega^2 B_1^+}. \quad (2.13)$$

2.1.4. INTEGRAL EQUATIONS

Instead of being based on Helmholtz equation, CSI-EPT is based on the electromagnetic integral equations.

The total field can be written as the addition of the incident field and the scattered field:

$$\mathbf{E}^{\text{tot}} = \mathbf{E}^{\text{inc}} + \mathbf{E}^{\text{sc}} \quad \text{and} \quad \mathbf{B}^{\text{tot}} = \mathbf{B}^{\text{inc}} + \mathbf{B}^{\text{sc}}, \quad (2.14)$$

for all $\mathbf{r} \in \mathbb{R}^2$, \mathbf{r} is the spatial variable. In the 2D configuration, only longitudinal component of electric field is considered. As a result, \mathbf{E} will not be a vector field any more.

According to domain integral equation [4], the scattered field can be represented as:

$$E^{\text{sc}} = \mathcal{G}w, \quad (2.15)$$

$$B_1^{+, \text{sc}} = \mathcal{G}^+ w, \quad (2.16)$$

where \mathcal{G} and \mathcal{G}^+ are electric current to electric field and electric current to transmit RF field Green's tensors respectively. Their mathematical representations will be introduced later. In addition, w is the contrast source which is defined as:

$$w = \chi E, \quad (2.17)$$

with χ the contrast function:

$$\chi = \varepsilon - j\frac{\sigma}{\omega\varepsilon_0} - 1. \quad (2.18)$$

According to the above equation, the electrical properties can be derived as:

$$\sigma = -\text{Im}(\chi + 1)\varepsilon_0\omega, \quad (2.19)$$

$$\varepsilon = \text{Re}(\chi + 1)\varepsilon_0, \quad (2.20)$$

where χ will be iteratively reconstructed through CSI-EPT method.

2.2. CONTRAST SOURCE INVERSION METHOD

CONTRAST Source Inversion (CSI) method reconstructs object's contrast and the total field simultaneously, by iteratively optimizing a cost function, which is defined as the addition of the discrepancy between measured field data and reconstructed field data and the object error. This section introduces some mathematical definitions and derivations of CSI-EPT. For more background, the reader can refer to [5].

First of all, the cost function is introduced, which is the addition of the normalized data residual and the normalized object residual:

Data residual:

$$\rho(\mathbf{r}) = B_1^{+;sc}(\mathbf{r}) - \mathcal{G}^+(\mathbf{r}) * w(\mathbf{r}), \quad (2.21a)$$

$$= B_1^+(\mathbf{r}) - B_1^{+;inc}(\mathbf{r}) - \mathcal{G}^+(\mathbf{r}) * w(\mathbf{r}), \quad \mathbf{r} \in \mathbb{S}, \quad (2.21b)$$

which is normalized as:

$$F_S(w) = \frac{\|\rho\|_{\mathbb{S}}^2}{\|B_1^{+;sc}\|_{\mathbb{S}}^2}, \quad (2.22)$$

\mathbb{S} denotes a bounded measurement domain.

Object residual:

$$r(\mathbf{r}) = \chi(\mathbf{r})E(\mathbf{r}) - w(\mathbf{r}) \quad (2.23a)$$

$$= \chi(\mathbf{r})E^{inc}(\mathbf{r}) - w(\mathbf{r}) + \chi\mathcal{G}(\mathbf{r}) * w(\mathbf{r}), \quad \mathbf{r} \in \mathbb{D}, \quad (2.23b)$$

which is normalized as:

$$F_D(w, \chi) = \frac{\|r\|_{\mathbb{D}}^2}{\|\chi E^{inc}\|_{\mathbb{D}}^2}, \quad (2.24)$$

\mathbb{D} denotes the object domain.

The above two residuals are normalized to make them both one when w is zero. The integration of multiple channels is embedded in the third dimension of the above variables, beside the two spatial dimensions.

For simplicity, the above denominators will be denoted by:

$$\eta_S = \frac{1}{\|B_1^{+;sc}\|_{\mathbb{S}}^2}, \quad \eta_D = \frac{1}{\|\chi E^{inc}\|_{\mathbb{D}}^2}. \quad (2.25a)$$

the total cost function becomes:

$$F(w, \chi) = F_S(w) + F_D(w, \chi) \quad (2.26a)$$

$$= \eta_S \|\rho\|_{\mathbb{S}}^2 + \eta_D \|r\|_{\mathbb{D}}^2 \quad (2.26b)$$

$$= \eta_S \|B_1^{+;sc} - \mathcal{G}^+ w\|_{\mathbb{S}}^2 + \eta_D \|\chi E^{inc} - w + \chi\mathcal{G}w\|_{\mathbb{D}}^2. \quad (2.26c)$$

The contrast source is updated via the gradient method:

$$w^{[n]} = w^{[n-1]} + \alpha^{[n]} v^{[n]}. \quad (2.27)$$

$v^{[n]}$ is the Polak-Ribière [6] update direction:

$$v^{[0]} = 0, \quad v^{[n]} = g^{[n]} + \frac{\operatorname{Re} \langle g^{[n]}, g^{[n]} - g^{[n-1]} \rangle_{\mathbb{D}}}{\|g^{[n-1]}\|_{\mathbb{D}}^2} v^{[n-1]}, \quad n \geq 1, \quad (2.28)$$

where $g^{[n]}$ is the gradient of the cost function from the last iteration 2.26c with respect to w . $g^{[n]}$ can be derived as:

$$g^{[n]} = \frac{\partial F(w^{[n-1]}, \chi^{[n-1]})}{\partial w^{[n-1]}} \quad (2.29a)$$

$$= -\eta_S \mathcal{G}^{+;*} \rho^{[n-1]} - \eta_D \mathcal{G}^* \bar{\chi}^{[n-1]} r^{[n-1]}. \quad (2.29b)$$

$\alpha^{[n]}$ is the step size and is obtained by minimizing the cost function $F(w, \chi)$:

$$\alpha^{[n]} = \operatorname{argmin}_{\alpha \in \mathbb{R}} F^{[n]}(w^{[n]}, \chi^{[n-1]}) \quad (2.30a)$$

$$= \operatorname{argmin}_{\alpha \in \mathbb{R}} \eta_S \|B_1^{+;sc} - \mathcal{G}^+ w^{[n]}\|_{\mathbb{S}}^2 + \eta_D \|\chi E^{\text{inc}} - w^{[n]} + \chi^{[n-1]} \mathcal{G} w^{[n]}\|_{\mathbb{D}}^2, \quad (2.30b)$$

replacing $w^{[n]}$ with eq. 2.27, leads to

$$\alpha^{[n]} = \frac{-\operatorname{Re} \langle g^{[n]}, v^{[n]} \rangle_{\mathbb{D}}}{\eta_S \|\mathcal{G}^+ v^{[n]}\|_{\mathbb{S}}^2 + \eta_D \|v^{[n]} - \chi^{[n-1]} \mathcal{G} v^{[n]}\|_{\mathbb{D}}^2}. \quad (2.31)$$

By combining eq. 2.27, 2.28 and 2.31, w can be updated. Then total electrical field can be updated according to integral equation:

$$E^{[n]} = E^{\text{inc}} + \mathcal{G} w^{[n]}. \quad (2.32)$$

Afterwards, the contrast can be updated by minimizing the object residual:

$$\chi^{[n]} = \operatorname{argmin}_{\chi \in \mathbb{C}} F_D^n(w^{[n]}, \chi) \quad (2.33a)$$

$$= \operatorname{argmin}_{\chi \in \mathbb{C}} \eta_D \|\chi E^{[n]} - w^{[n]}\|_{\mathbb{D}}^2, \quad (2.33b)$$

which leads to

$$\langle \chi E^{[n]} - w^{[n]}, \bar{E}^{[n]} \rangle_{\mathbb{D}} = 0. \quad (2.34)$$

The minimizer of above equation is the contrast we want

$$\chi^{[n]} = \frac{w^{[n]} \bar{E}^{[n]}}{E^{[n]} \bar{E}^{[n]}}. \quad (2.35)$$

2.2.1. INITIAL CONDITION

The initial condition of contrast source is determined by minimizing the data error with respect to $w^{[0]}$. The cost function is

$$F_S(w^{[0]}) = \eta_S \|B_1^{+;sc} - \mathcal{G}^+ w^{[0]}\|_{\mathbb{S}}^2, \quad (2.36)$$

Applying the gradient method, we get

$$w^{[0]} = \alpha_w \partial w^{[0]}, \quad (2.37)$$

with the gradient

$$\partial w^{[0]} = \mathcal{G}^{+;*} B_1^{+;sc}. \quad (2.38)$$

The step size is obtained by minimizing the initial cost function 2.36

$$\alpha_w = \underset{\alpha_w \in \mathbb{R}}{\operatorname{argmin}} \eta_S \| B_1^{+;sc} - \mathcal{G}^+ \alpha_w \partial w^{[0]} \|_{\mathbb{S}}^2. \quad (2.39)$$

This leads to

$$\langle B_1^{+;sc} - \mathcal{G}^+ \alpha_w \partial w^{[0]}, \mathcal{G}^+ \partial w^{[0]} \rangle_{\mathbb{S}} = 0, \quad (2.40)$$

then it comes to the step size

$$\alpha_w = \frac{\langle B_1^{+;sc}, \mathcal{G}^+ \partial w^{[0]} \rangle_{\mathbb{S}}}{\| \mathcal{G}^+ \partial w^{[0]} \|_{\mathbb{S}}^2}, \quad (2.41)$$

replace the gradient according to eq. 2.38 and take use of the definition of adjoint,

$$\alpha_w = \frac{\| \mathcal{G}^{+;*} B_1^{+;sc} \|_{\mathbb{S}}^2}{\| \mathcal{G}^+ \mathcal{G}^{+;*} B_1^{+;sc} \|_{\mathbb{S}}^2}. \quad (2.42)$$

Finally, combine the gradient from eq. 2.38 and the step size from eq. 2.42 $w^{[0]}$ is obtained as

$$w^{[0]} = \frac{\| \mathcal{G}^{+;*} B_1^{+;sc} \|_{\mathbb{S}}^2}{\| \mathcal{G}^+ \mathcal{G}^{+;*} B_1^{+;sc} \|_{\mathbb{S}}^2} \mathcal{G}^{+;*} B_1^{+;sc}. \quad (2.43)$$

2.2.2. GREEN'S TENSORS

The electric current to magnetic field and electric to electric field Green's tensors at 2D are derived from Maxwell equations. The mathematical expressions are shown below:

$$\mathcal{G}^+ = j\omega\mu_0\varepsilon_b \frac{\nabla g_y - j\nabla g_x}{2}, \quad (2.44a)$$

$$\mathcal{G}^- = j\omega\mu_0\varepsilon_b \frac{\nabla g_y + j\nabla g_x}{2}, \quad (2.44b)$$

$$\mathcal{G}^{+;*} = j\omega\mu_0\varepsilon_b \frac{\nabla g_y^* + j\nabla g_x^*}{2}, \quad (2.44c)$$

$$\mathcal{G}^{-;*} = j\omega\mu_0\varepsilon_b \frac{\nabla g_y^* - j\nabla g_x^*}{2}, \quad (2.44d)$$

$$\mathcal{G} = k_b^2 g. \quad (2.44e)$$

for all $\mathbf{r} \in \mathbb{R}^2$, where g is the Green's function, k_b is the constant complex wave number of background medium, with $\operatorname{Im}\{k_b\} \leq 0, \operatorname{Re}\{k_b\} = \omega[\mu_0\varepsilon_b]^{1/2}$. The derivations can be found in [7] [1].

The Green's functions in time domain can be written as [8]:

$$g(\mathbf{r}_{m,n} - \mathbf{r}'_{m',n'}) = \begin{cases} -\frac{j}{k_b \Delta r} [H_1^{(2)}(\frac{1}{2} k_b \Delta r) - \frac{4j}{\pi k_b \Delta r}] & \forall \mathbf{r}_{m,n} = \mathbf{r}'_{m',n'} \\ -\frac{j}{k_b \Delta r} J_1(\frac{1}{2} k_b \Delta r) H_0^{(2)}(k_b |\mathbf{r}_{m,n} - \mathbf{r}'_{m',n'}|) & \forall \mathbf{r}_{m,n} \neq \mathbf{r}'_{m',n'} \end{cases} \quad (2.45)$$

$$\nabla g(\mathbf{r}_{m,n} - \mathbf{r}'_{m',n'}) = \begin{cases} 0 & \forall \mathbf{r}_{m,n} = \mathbf{r}'_{m',n'} \\ \frac{j}{\Delta r} J_1(\frac{1}{2} k_b \Delta r) H_1^{(2)}(k_b |\mathbf{r}_{m,n} - \mathbf{r}'_{m',n'}|) \frac{\mathbf{r}_{m,n} - \mathbf{r}'_{m',n'}}{|\mathbf{r}_{m,n} - \mathbf{r}'_{m',n'}|} & \forall \mathbf{r}_{m,n} \neq \mathbf{r}'_{m',n'} \end{cases} \quad (2.46)$$

where $H_0^{(2)}$ and $H_1^{(2)}$ are Bessel functions.

REFERENCES

- [1] J. Jin *et al.*, *Computation of electromagnetic fields for high-frequency magnetic resonance imaging applications*, *Physics in Medicine Biology* **41**, 2719 (1996).
- [2] D. Hoult, *The principle of reciprocity in signal strength calculations - a mathematical guide*, *Concepts in Magnetic Resonance* **12**, 173 (2000).
- [3] M. Vaidya *et al.*, *Dependence of B_1^+ and B_1^- field patterns of surface coils on the electrical properties of the sample and the MR operating frequency*, *Concepts in Magnetic Resonance Part B: Magnetic Resonance Engineering* **46**, 25 (2016).
- [4] A. T. de Hoop, *Handbook of radiation and scattering of waves*, San Diego, CA: Academic (1995).
- [5] A. Abubakar, *Three-dimensional nonlinear inversion of electrical conductivity*, PhD Thesis at TU Delft (2000).
- [6] E. Balidemaj *et al.*, *CSI-EPT: A contrast source inversion approach for improved MRI-based electric properties tomography*, *IEEE Transactions on Medical Imaging* **34**, 1788 (2015).
- [7] R. F. Remis *et al.*, *Wave field imaging lecture notes*, Teaching material at TU Delft , 9 (2016).
- [8] W. M. Brink *et al.*, *Non-invasive electromagnetic ablation of female breast tumors*, Master Thesis at TU Delft (2010).

3

GENERAL CONFIGURATION

This chapter describes the experimental and numerical setup.

This chapter presents the general configurations that will be used in subsequent investigations, from simulation aspects to experimental aspects.

3.1. EXPERIMENTAL SETUP

Since the goal of this project is to explore the experimental feasibility of CSI-EPT, we also study on acquired data besides simulation. This section presents some details about the experimental setup.

MR SCANNER

Experimental data will be acquired on a 7 Tesla whole body MRI system of Philips, at the C. J. Gorter Center, Leiden University Medical Center, Leiden, the Netherlands. The system is equipped with eight-channel RF transmit setup, enabling channel-wise experiments.

PHANTOM

The experimental scans are conducted in a phantom, which mimics the human calf. The phantom is a cylindrical plastic container ($L = 40$ cm, $D = 10$ cm) filled with prepared solution, and it is compounded according to the recipe: 100 g water, 0.5 g NaCl, 40 g PVP (Polyvinylpyrrolidone), to achieve EPs of $\epsilon_r = 60$, $\sigma = 0.65S/m$, which are close to the electrical properties of muscle at 300 MHz (Larmor frequency at 7T).

RF COIL

A four-channel dipole array is implemented in our experiments. In transceive mode of operation, transmission is done by each channel sequentially, and reception is done by the four channels altogether in quadrature mode. We apply this transceive mode to avoid low E-field issue of birdcage mode and to lower the difficulty of transmit phase correcting by improving the uniformity of the receive phase map.

The implemented dipole array is designed also by us via a Remcom-MATLAB circuit co-simulation method, where the dipoles are segmented and the inductors' positions and values are subsequently optimized in terms of central transmit efficiency, SNR and SAR efficiency. More information about the design of the dipole array is presented in [1].

A simulated model and a picture of the implemented phantom and dipole array is shown in fig. 3.5b

MR SEQUENCE

The method DREAM (dual refocusing echo acquisition) is used for B_1^+ acquisitions in this project [2]. DREAM provides B_1^+ amplitude and transceive phase with sufficient quality at high speed (about 100 to 300 ms/slice). This method takes use of a STEAM magnetization preparation sequence, then generates a stimulated echo (STE) and a free induction decay (FID) echo,

$$I_{STE} = \frac{1}{2} \sin(\beta) \sin^2(\alpha) \cdot M_0, \quad (3.1)$$

$$I_{FID} = \sin(\beta) \cos^2(\alpha) \cdot M_0, \quad (3.2)$$

according to which, the B_1 amplitude and transceive phase can be obtained as:

$$|B_1^+| = \frac{\arctan \sqrt{2|I_{STE}/I_{FID}}}{\alpha}, \quad (3.3a)$$

$$\phi^\pm = \frac{\arg(I_{FID} \cdot I_{STE})}{2}, \quad (3.3b)$$

where α is the nominal flip angle of STEAM pulse, I_{STE} and I_{FID} are STE and FID signals respectively.

EDDY CURRENT EFFECT COMPENSATION

After the first acquisition, we perform a second acquisition with the reversed readout gradient, which is a conventional method for eddy current effect compensation.

Eddy current may induce an additional phase term in acquired B_1 phase data, which can be characterized by the equation [3]:

$$\phi_{\text{eddy}}(\mathbf{r}) = \gamma \int_0^{\text{TE}} \Delta B_{\text{eddy}}(\mathbf{r}, t), \quad \mathbf{r} \in \mathbb{S}, \quad (3.4)$$

where γ is gyromagnetic ratio, TE is echo time, $\Delta B_{\text{eddy}}(\mathbf{r}, t)$ is the eddy current field. Then the total phase accumulation when implementing either positive or negative readout gradient can be expressed as:

$$\phi_{\text{positive}}^\pm(\mathbf{r}) = \phi_{\text{data}}^\pm(\mathbf{r}) + \phi_{\text{eddy}}(\mathbf{r}), \quad (3.5a)$$

$$\phi_{\text{negative}}^\pm(\mathbf{r}) = \phi_{\text{data}}^\pm(\mathbf{r}) - \phi_{\text{eddy}}(\mathbf{r}). \quad (3.5b)$$

As a result, to compensate for the residual gradient of phase map that is induced by eddy currents, a second acquisition with reversed readout gradient can be conducted. By doing so, the average of those two phase maps will be clean from eddy current effect, and half of the difference represents the phase due to the eddy currents. The above process can be written as:

$$\phi_{\text{data}}^\pm(\mathbf{r}) = \frac{\phi_{\text{positive}}^\pm(\mathbf{r}) + \phi_{\text{negative}}^\pm(\mathbf{r})}{2}, \quad (3.6a)$$

$$\phi_{\text{eddy}}(\mathbf{r}) = \frac{\phi_{\text{positive}}^\pm(\mathbf{r}) - \phi_{\text{negative}}^\pm(\mathbf{r})}{2}, \quad (3.6b)$$

For example, as shown in fig. 3.1, the image on the left shows a measured transceive phase map with our experimental setup; the image in the middle shows the second measurement with a reversed readout gradient; the image on the right shows the transceive phase that is simulated on the 2D model. All the three phase maps should represent transceive phase of the center slice of the phantom at $7T$, but they appear very different, due to the eddy current effect. It can be observed that there is a strong extra gradient along the transverse, and the gradient changes as readout gradient changes.

The experimental data after the compensation is shown in fig. 3.2, where we can see the compensated data has a high similarity to the simulation. In addition, eddy current effects are not always so strong as figure 3.2 shows. It depends on echo time, gradient waveforms and magnetic field strength.

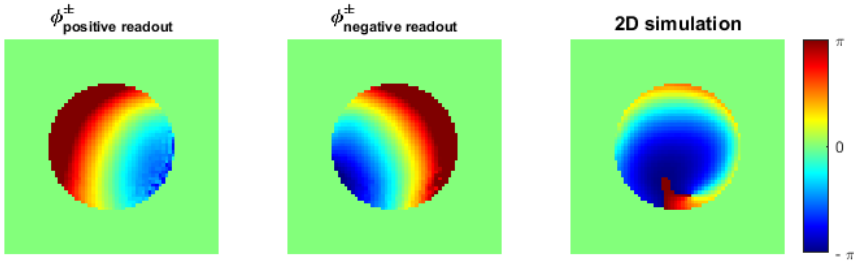


Figure 3.1: Acquired transceive phase maps with two opposite readout gradients along with corresponding simulation reference of a single channel. Transceive mode: channel-wise transmission and quadrature reception based on a four-channel dipole array. Colormap range: $[-\pi, \pi]$.

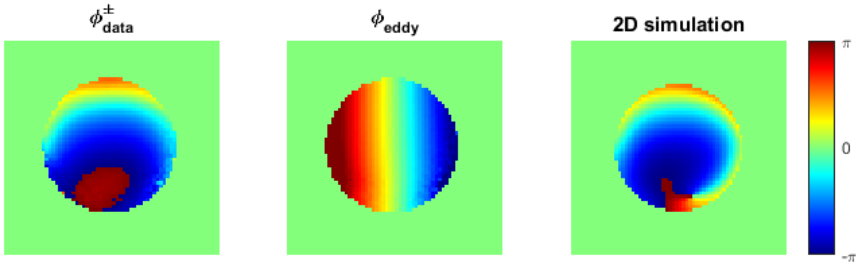


Figure 3.2: Acquired phase maps after eddy-current effect compensation, eddy current induced residual phase gradient, simulation reference.

3.2. SIMULATION SETUP

Simulation studies of this project are based on two models: a 2D model based on integral equations implemented in MATLAB (MathWorks, Natick, Massachusetts, USA) and a 3D model implemented in XFDTD (Remcom inc., State College, PA, USA). This section introduces these two models and the associated principles.

2D MODEL

The 2D model approximates the 3D configuration by assuming longitudinal invariance. The object phantom is modeled by a disk region with constant dielectric properties ($\sigma = 0.65$ S/m, $\epsilon_r = 60$) inside. The dipole array is modeled by line sources surrounding the phantom. The size of phantom, the allocation of dipoles, the magnetic field strength and the contrast within phantom can be customized flexibly according to the experimental setup. The electrical properties' maps of the 2D object are shown in fig. 3.3. Fig. 3.4 shows the estimated incident B_1^+ fields at $7T$, where the amplitude peaks correspond to the positions of dipoles. With these incident fields and contrast, the total field will be generated by resolving a forward scattering problem, according to the electromagnetic integral equations. The simulated total field by 2D model will serve as input to guide CSI-EPT reconstructions; It will also provide a good reference for experimental studies.

Most importantly, it is the backbone of 2D CSI-EPT.

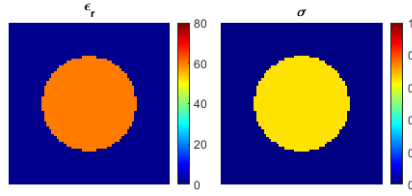


Figure 3.3: 2D object model. $r_{\text{phantom}} = 5 \text{ cm}$, $\epsilon_r = 60$, $\sigma = 0.65$, resolution = $2.5 \times 2.5 \text{ mm}^2$.

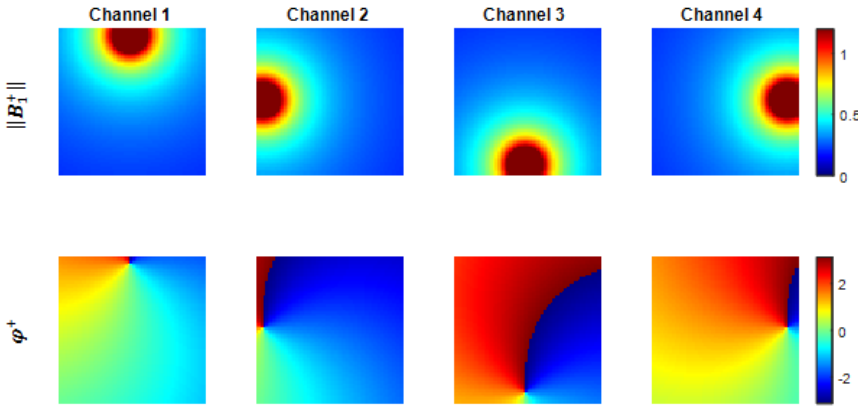


Figure 3.4: Incident transmit field of a four-channel dipole array. $r_{\text{array}} = 7.5 \text{ cm}$, $B_0 = 7 \text{ T}$, resolution = $2.5 \times 2.5 \text{ mm}^2$.

NOISE INCORPORATION AND SNR DEFINITION

When incorporating noise in our simulated fields, we define an additive noise as:

$$N = N_{\text{RE}} + jN_{\text{IM}}, \quad (3.7)$$

where N_{RE} and N_{IM} are independent Gaussian noise with identical distribution:

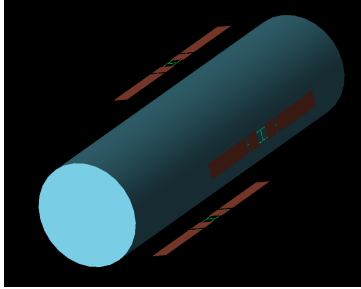
$$N_{\text{RE}} \sim \mathcal{N}(0, \sigma^2), N_{\text{IM}} \sim \mathcal{N}(0, \sigma^2). \quad (3.8)$$

While in actual acquisition, the noise is more complicated. In addition, we relate SNR to σ as $\text{SNR} = \frac{\max \|B_1^+\|}{\sigma}$.

In the next chapter, we will incorporate the above noise with varying SNR to the 2D simulation, not to model or compare with actual measurement, but to do a parallel comparison between different transceive modes and reconstructing algorithms. To make this comparison fair as possible, the noise will be added dipole-wisely, for both channel-wise transceive mode and quadrature transceive mode, which means, to quadrature mode, the noise will be added to each channel before being combined in quadrature mode.

3D MODEL

Beside 2D simulation, we incorporate also a 3D simulation model using XFDTD (Remcom inc., State College, PA, USA), where we can build a 3D geometry. The EM simulation from this 3D model provides another reference besides 2D simulations. The 3D model is shown in fig. 3.5a.



(a) A model by XFDTD, mimicing the condition in reality.

(b) Picture of the phantom and the dipole array.

Figure 3.5: Model display.

REFERENCES

- [1] W. Brink *et al.*, *Dielectric enhanced dipoles for mri - approaching the ideal current pattern*, ICEAA - IEEE APWC (2017).
- [2] P. Börnert *et al.*, *DREAM - a novel approach for robust, ultrafast, multislice B_1 mapping*, *Magnetic Resonance in Medicine* **68**, 1517 (2012).
- [3] S. Mandija *et al.*, *A geometrical shift results in erroneous appearance of low frequency tissue eddy current induced phase maps*, *Magnetic Resonance in Medicine* **76**, 905 (2016).

4

SIMULATION STUDIES

This chapter investigates CSI-EPT through simulations based on the 2D configuration.

This chapter investigates CSI-EPT through simulations, which can be divided into three parts: regular CSI-EPT with exact transmit phase input, regular CSI-EPT implementing Transmit Phase Assumption, Transmit Phase Correcting CSI-EPT. The investigation varies not only the input and algorithm, also SNR, target size and transceive modes. The simulations are based on a 2D model which approximates the actual condition with a cylindrical object and four line sources. The simulation setup has been presented in the third chapter.

In addition, two excitation modes will be performed on the four-channel dipole array for RF signal transmission and reception: channel-wise mode and quadrature mode. These two modes will be implemented both in simulations and experiments throughout this thesis. The first mode generates a linearly polarized incident RF field, and the second mode generates a circularly polarized incident RF field.

4.1. REGULAR CSI-EPT WITH TRANSMIT PHASE INPUT

This section investigates regular CSI-EPT with exact transmit data input, in terms of field maps and CSI-EPT reconstructions, by varying three variables: transceive modes, conductivity, and SNR. Although regular CSI-EPT only takes transmit fields into account, this section will also present some observations about receive fields when investigating field maps, to give some preliminary knowledge relevant to subsequent sections.

4.1.1. CHANNEL-WISE TRANSMISSION AND RECEPTION

This transceive mode excites each dipole sequentially both for transmission and reception. To compensate the region that is far away from each single dipole (especially opposite side), where much weaker signal can be generated comparing to most other regions, four dipoles are used sequentially. As aforementioned, exciting a single dipole can produce a linearly polarized field in free space [1], however, the sample-induced conduction currents reduce the linearity and make the field polarization elliptical [2]. As a result, an asymmetric rotating B_1 field will be observed, as shown in fig. 4.1. Because of the low conductivity and relatively low magnetic strength, the target has a weak interaction with the incident field, so the scattered field is very similar to the incident field, with almost symmetric amplitude maps and nearly linear phase maps. As σ increases, the RF interactions with the sample become more pronounced, resulting in the arising asymmetry of amplitude maps and the twisting of phase maps. Furthermore, when B_0 is increased to 7 T, with a default relative permittivity 60, the wavelength is around 0.13 m according to $\lambda = \frac{\lambda_0}{\sqrt{\epsilon_r}}$, which is comparable to the target size 0.1 m (diameter). Therefore, the scattering between electromagnetic waves and the target becomes significant, and it twists the B_1 fields further. Another important observation from fig. 4.1 is that, when exciting a single dipole, transmit fields mirror receive fields with respect to the central axis of the coil, which can be attributed to the opposing polarization [2].

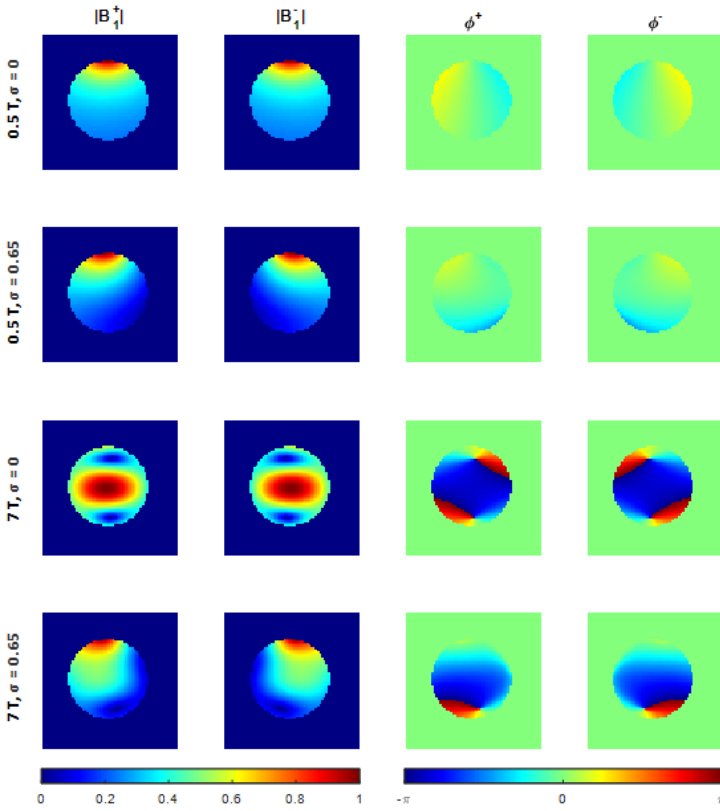


Figure 4.1: Field maps when implementing a single channel.

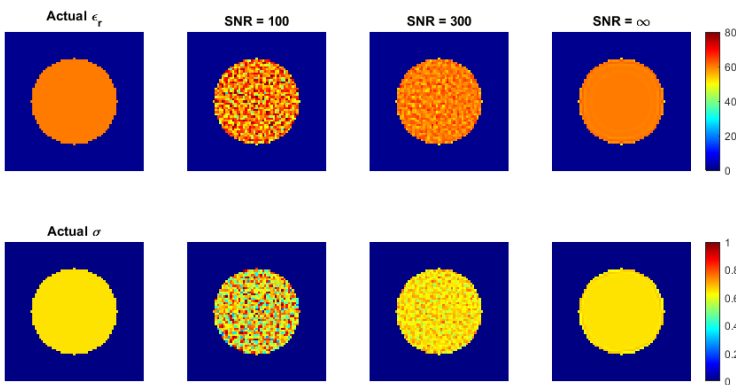


Figure 4.2: Regular CSI-EPT reconstructions with synthetic channel-wise transmit field data input.

However, when considering regular CSI-EPT, only transmit fields are relevant, for which reason the transceive mode channel-wise for transmission and quadrature for reception will not be specifically discussed about in regular CSI-EPT. Fig. 4.2 shows the reconstructed electrical properties by regular CSI-EPT, when feeding synthetic transmit fields of four separate channels under 7T, with different level of synthetic noise. The noise model has been presented in the third chapter.

4.1.2. QUADRATURE MODE FOR TRANSMISSION AND RECEPTION

As mentioned in the second chapter 2.1.1, activating two perpendicular magnetic field components with the same amplitude and 90° phase delay produces a circularly polarized field in free space. Moreover, if the target's geometry and electrical properties are equivalent from the sight of each linear field source (eg. a homogeneous circle, a square with certain antenna placement, etc.), the scattering between the target and electromagnetic waves of two orthogonal linear fields will cancel-out each other [3]. In another word, if the target is symmetric in terms of both geometry and electrical properties, with respect to at least two different axes, it can maintain the circularity of incident field, under certain field source placement, and be free from the target-EM wave scattering interference. The field maps when using quadrature excitation are shown in the first line of fig. 4.3, with constructive transmit amplitude and homogeneous transmit phase; the field maps when using the reversal quadrature excitation is shown in the second line of fig. ??, with constructive receive amplitude and uniform receive phase. It can be observed that, the asymmetry of each single channel is cancelled out. Additionally, transmit field under quadrature excitation ($B_{1,\text{quad}}^+$) and receive field under anti-quadrature excitation ($B_{1,\text{anti-quad}}^-$) have a high correspondence with each other. This mode of excitation and reception corresponds to the use of quadrature birdcage, which has been used in conventional EPT methods.

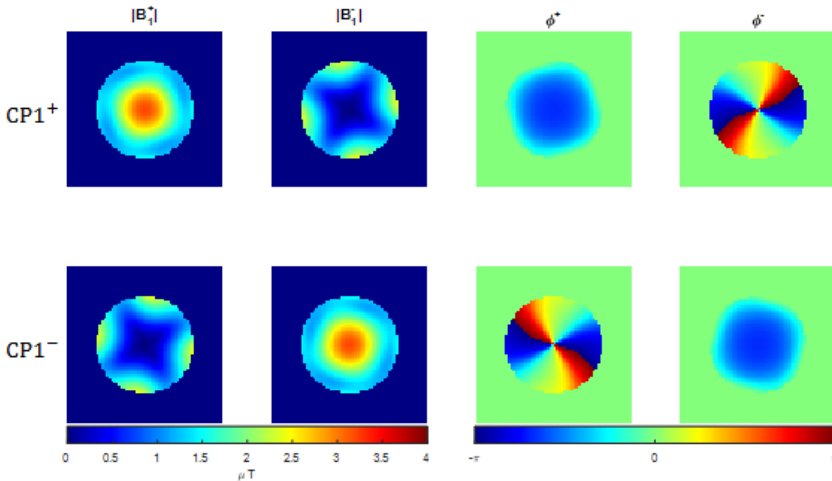


Figure 4.3: Field maps when using quadrature and anti-quadrature excitation on two pairs of opposite dipoles.

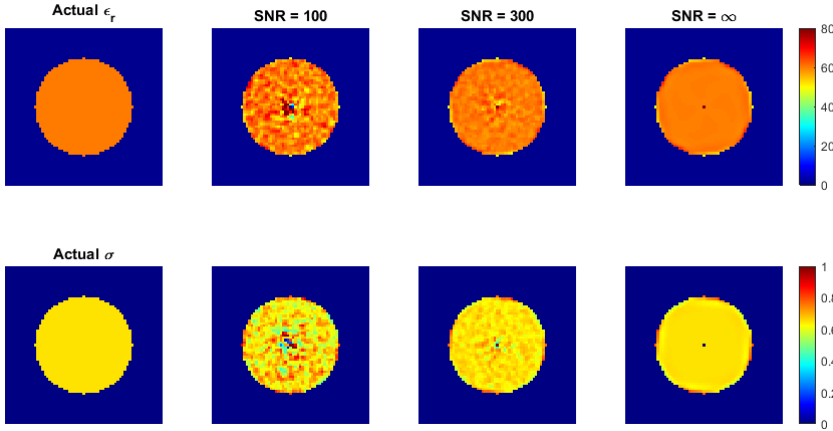


Figure 4.4: Regular CSI-EPT reconstruction when feeding synthetic transmit fields generated by quadrature excitation.

On the other hand, the reconstruction by regular CSI-EPT when using $B_{1,\text{quad}}^+$ as input data is simulated, as shown in fig. 4.4. As we can see, the center region is corrupted more than other regions, which is the so-called low E-field issue. As introduced in the second chapter, during the updating procedure of CSI-EPT, the reconstruction of the contrast χ relies on the electric field at that position, which is also reconstructed during each iteration. Therefore, at regions with low E-field, the algorithm loses sensitivity. While quadrature mode happens to have a low E-field region at the center due to the symmetric geometry - the E-fields generated by opposite antennas cancel each other. Moreover, the noise will spread the low E-field effect, which can be observed from fig. 4.4. When the environment is free of noise, with a homogeneous cylindrical object, the low E-field issue appears as a single pixel's corruption at the center; as noise increases, the corrupted area increases in size.

However, transmit phase haven't been able to be measured exactly by any published acquiring methods. The next two sections describes two methods to handel this limitation: Transceive Phase Assumption and Transmit Phase Correcting CSI-EPT.

4.2. REGULAR CSI-EPT IMPLEMENTING TRANSCIVE PHASE ASSUMPTION

The first application of EPT is in 2003 by Wen *et al.* [4], where they approximate the transmit phase by half of the acquired phase (transceive phase), which is the so-called Transceive Phase Assumption (TPA). Most EPT methods rely on TPA when it comes to application. TPA is based on the assumption that ϕ^+ and ϕ^- are equal under certain conditions [3]. Mathematically, TPA is represented as [3]:

$$\phi^{TPA}(\mathbf{r}) = \frac{\phi^\pm(\mathbf{r})}{2}. \quad (4.1)$$

It is commonly acknowledged that, TPA only holds under two certain conditions: linear polarization, and quadrature excitation with reversal of quadrature combination in transmit and receive (usually on two ports of a birdcage) [3]. In this section, we evaluate TPA in terms of field maps and corresponding CSI-EPT reconstructions, under the same two transceive modes as before, which are believed to be approaching the two modes that support TPA.

4.2.1. CHANNEL-WISE TRANSMISSION AND RECEPTION

As stated in the last section, exciting a single dipole can produce a linearly polarized field in free space, where the electrical conductivity is zero. Recall the phase maps of a single channel, as we can see from fig. 4.5, the linearity of phase maps are corrupted when there is an object ($\sigma = 0.65$ S/m). Moreover, when there is no object ($\sigma = 0$ S/m), which means the field is linearly polarized, ϕ^+ has a correspondence with $-\phi^-$, as shown in the first line of fig. 4.5. Therefore, transmit phase is equal to half of the difference between transmit and receive fields ($\phi^+ = \frac{\phi^+ - \phi^-}{2}$) in linearly polarized fields, but not half the summation (transceive phase, the acquired phase). As a result, there is no TPA when the field is linearly polarized. More explanations from the mathematical aspects can be found in the appendix A.

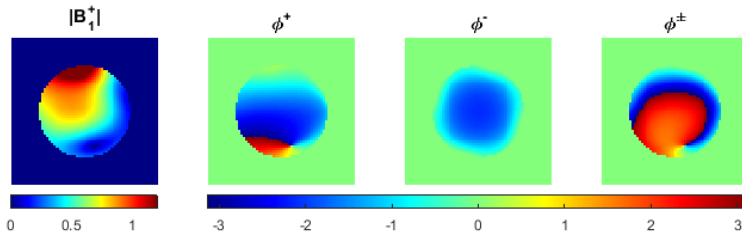


Figure 4.6: Transmit fields when implementing channel-wise transmission and quadrature reception.

Besides, since the transmit field and the receive field when implementing channel-wise transmission and quadrature reception are completely different, as shown in fig. 4.6, Transmit Phase Assumption is not possible to be valid under this transceive mode, therefore no further discussion.

4.2.2. QUADRATURE EXCITATION FOR TRANSMISSION AND ANTI-QUADRATURE FOR RECEPTION

In addition to linear polarization mode, combination of quadrature and anti-quadrature excitation is also believed to suit TPA [3]. As discussed in the last section, we observed high correspondence between $B_{1,\text{quad}}^+$ and $B_{1,\text{anti-quad}}^-$. Recall the phase maps and perform TPA, the results are presented as fig. 4.7. From these figures, it can be observed that, the error in the TPA is non-negligible. For more objective description of the deviation, a ratio map is also used beside the map of difference. As we can see, the error is mainly distributed at the edge, as a result of insufficient circular symmetry of the four

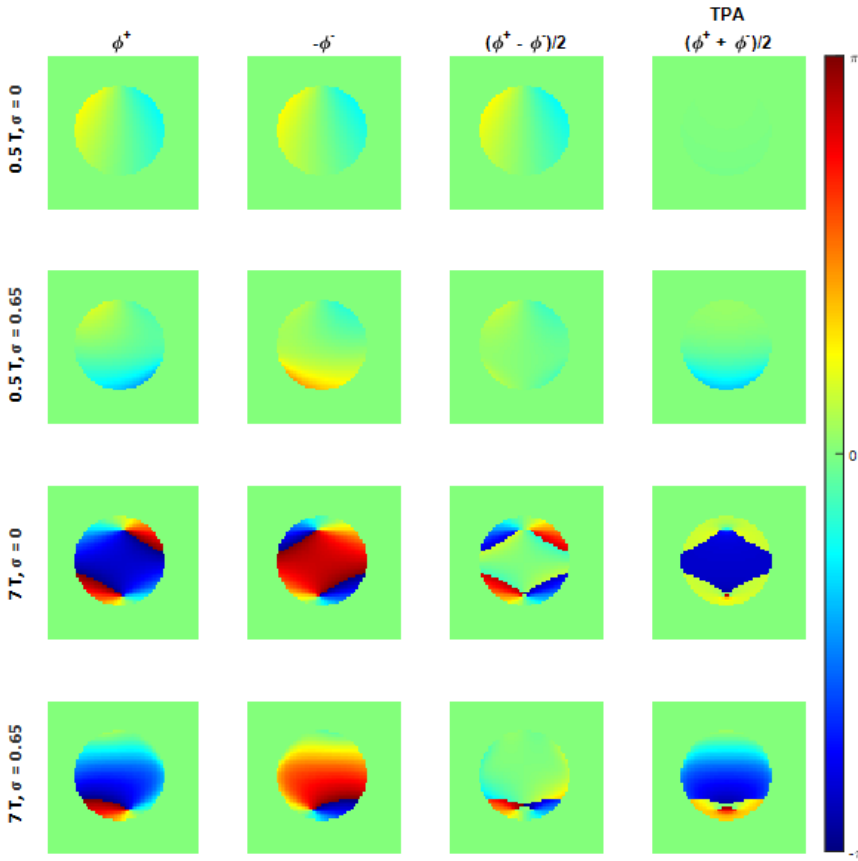


Figure 4.5: TPA implementation with single dipole excitation.

channel dipole array, and it is consistent as the magnetic field and the object's electrical conductivity change. The error will be improved when implementing a birdcage or a dipole array with more channels. For example, an eight-channel dipole array would be sufficient. It can also be observed that, the performance of TPA is increased as the electrical conductivity or the main magnetic field strength increases, because the errors due to transceive elements' geometry (peripheral errors) become less obvious when phase maps themselves become more pronounced.

Besides field maps, we are also curious about the performance of TPA in terms of CSI-EPT reconstruction. We input B_1^+ data with ϕ^{TPA} into regular CSI-EPT, at three conditions, which are consistent with field map investigation. The performance is evaluated by taking the ratio between the actual electrical properties and the reconstructed electrical properties. It can be observed that, the error in phase map is spatially transported to reconstructed maps. Moreover, the error is amplified in reconstruction, as shown in figure 4.8. Besides, there is no reconstruction for conductivity when the object's electrical

conductivity is too low, as the conductivity reconstruction when $\sigma = 0$ S/m.

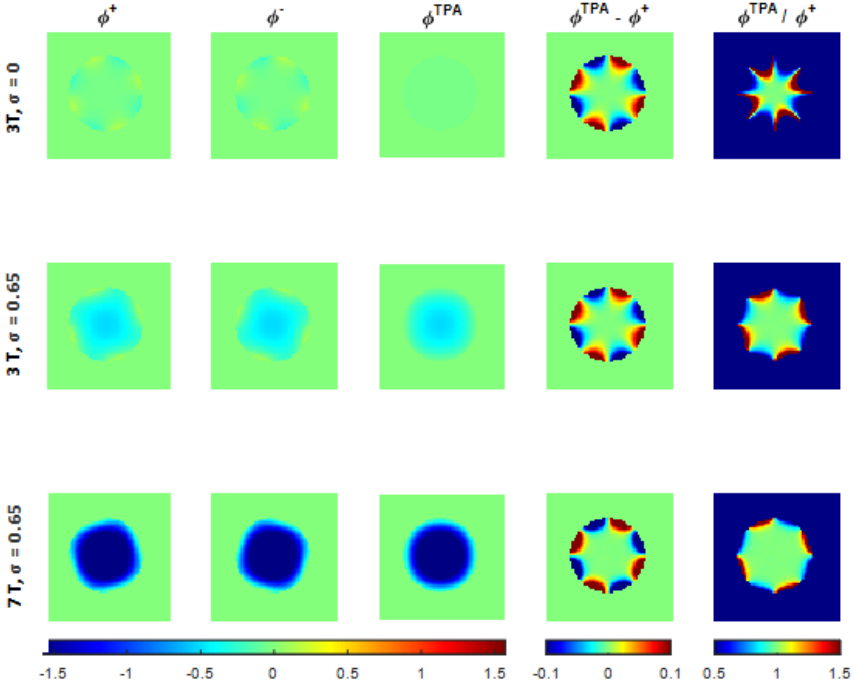


Figure 4.7: Phase maps and TPA when using quadrature and anti-quadrature excitation sequentially.

Therefore, when implementing combination of quadrature and anti-quadrature excitation, the performance of TPA increases as field strength increases, where stronger signal would be generated. However, under this excitation mode, the circularity of field polarization would be spoiled if the target is not highly symmetric (at least a square, a circle would be perfect), in terms of both geometry and electrical properties, which is impractical in vivo. As long as the circularity is corrupted, scattering effects arises, then high field strength loses advantage by leading to more scattering.

4.3. TRANSMIT PHASE CORRECTING CSI-EPT

Beside Transceive Phase Assumption, we are introducing another idea to retrieve the transmit phase. We modify the cost function by formulating the acquired phase data as transceive phase, and update the transceive phase through transmit phase reconstruction, which leads to a different data residual:

$$\rho = \| B_1^+ \| e^{j\phi^\pm} - G^+ w_n e^{\phi_n^-}. \quad (4.2)$$

It is equivalent to:

$$\rho = \| B_1^+ \| e^{j(\phi^\pm - \phi_n^-)} - G^+ w_n. \quad (4.3)$$

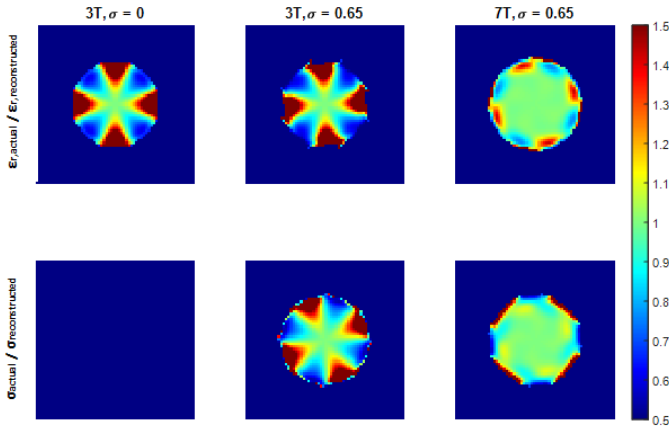


Figure 4.8: Performance of reconstruction by regular CSI-EPT implementing TPA. Iteration number = 200.

4.3.1. PERFORMANCE

We evaluate the performance of Transmit Phase Correcting CSI-EPT under three transceive modes: channel-wise transmission and reception, channel-wise transmission and quadrature reception, quadrature transmission and reception. The reconstructed result is shown in fig. 4.9. We can see that, after 200 iterations, channel-wise Tx and quadrature Rx mode leads to a high-quality reconstruction of electrical properties; quadrature TxRx mode performs relatively well comparing to channel-wise TxRx, which is far away from actual data. In addition, some fluctuations have been observed during the above reconstructions, for which reason we also refer to the cost function curves, as shown in fig. 4.10. The curves demonstrate the updating procedure in terms of the cost functions, including the normalized data residual and object residual, and their addition, which is the total cost function. It can be observed from fig. 4.10 that, under channel-wise TxRx mode, the reconstruction is unstable, with a lot of divergence; under channel-wise Tx and quadrature Rx mode, the cost functions generally converge, with a few divergences occurring before 50 iterations; under quadrature TxRx mode, the data residual converges without fluctuation, and the object residual stays at an extremely low level from the beginning. Although quadrature TxRx mode leads to the most stable convergence, channel-wise Tx and quadrature Rx mode reaches a lower error after 200 iterations ($F = 2 \times 10^{-6}$), comparing to that of quadrature TxRx mode ($F = 8 \times 10^{-6}$), which means a better reconstructed result.

4.3.2. ROBUSTNESS

As shown in last section, Transmit Phase Correcting CSI-EPT works successfully in our synthetic environment, but its robustness still needs to be evaluated before we call it a solution to the absence of transmit phase. This section tests the robustness of Transmit Phase Correcting CSI-EPT algorithm by varying SNR of input data, and by including boundaries of target's electrical properties. Since it has been proved in last section that,

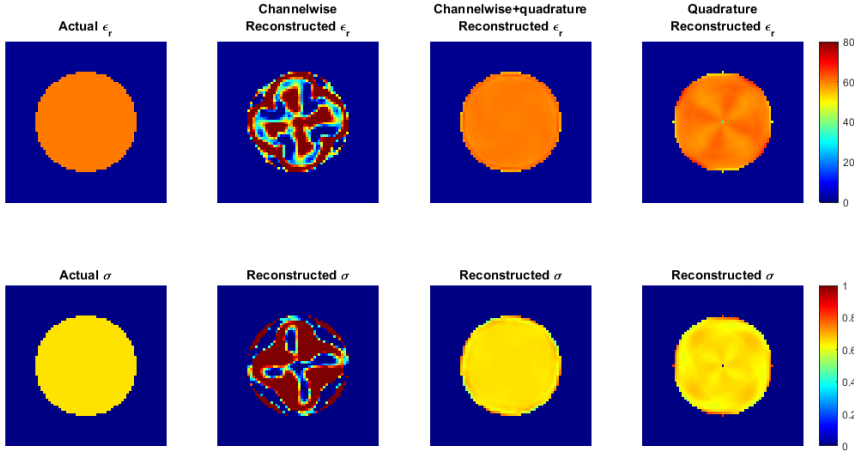


Figure 4.9: Transmit Phase Correcting CSI-EPT reconstruction under three different transceive modes, after 200 iterations.

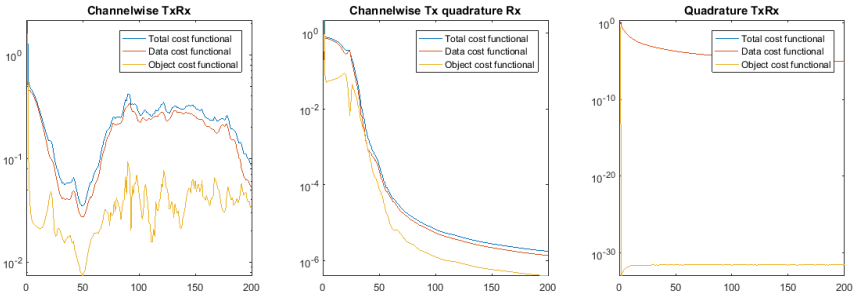


Figure 4.10: Updating of the cost functions when performing Transmit Phase Correcting CSI-EPT under three different transceive modes.

channel-wise TxRx mode has a severe stability issue, the evaluation of this part is only under the other two transceive modes: channel-wise Tx and quadrature Rx, and quadrature TxRx.

The reconstructed results when including noise are shown in fig. 4.11 and fig. 4.12. From visually observation, it seems like the noise tolerance of Transmit Phase Correcting CSI-EPT is not worse than regular CSI-EPT. It appears like Transmit Phase Correcting CSI-EPT even smooths the noise, comparing to regular CSI-EPT. However, in terms of the standard deviation of reconstructed results, we haven't observed any obvious advantage of either methods, after evaluating ten runs. Besides, the low E-field issue of quadrature TxRx mode can be observed arising as noise level increases.

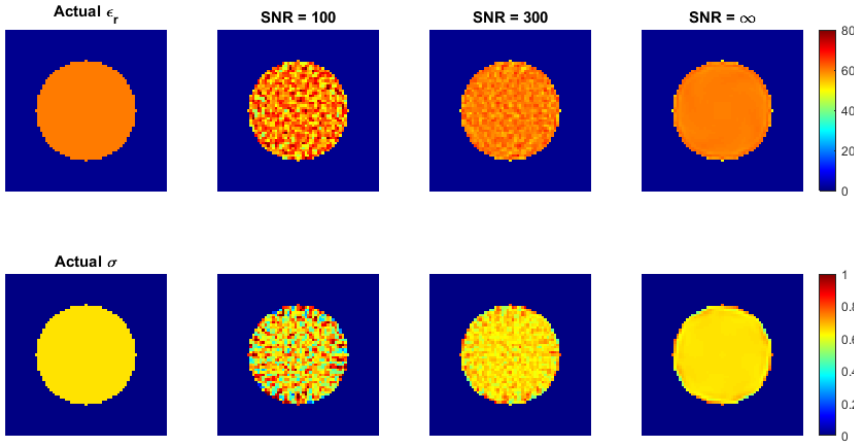


Figure 4.11: Transmit Phase Correcting CSI-EPT under channel-wise Tx and quadrature Rx mode, after 200 iterations.

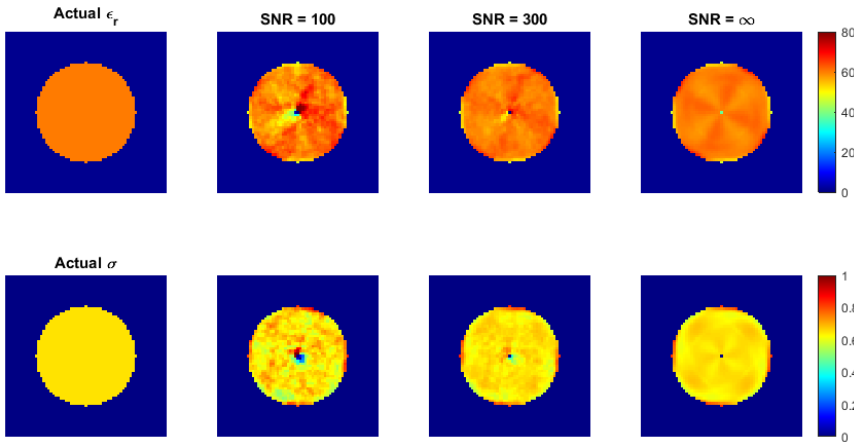


Figure 4.12: Transmit Phase Correcting CSI-EPT under quadrature TxRx mode, after 200 iterations.

The performance on handling boundaries of electrical properties is also of our concern, to test which we implement a synthetic head model. In order to fit the head model, which is larger than the former cylindrical phantom, the size of dipole array and the number of dipoles are both doubled. Fig. 4.13 shows three groups of reconstructed results by: regular CSI-EPT with transmit phase input, under channel-wise Tx mode; Transmit Phase Correcting CSI-EPT under channel-wise Tx and quadrature Rx mode; regular CSI-EPT under quadrature TxRx mode using TPA. The reconstruction by Transmit Phase Correcting CSI-EPT under quadrature TxRx mode is not included here, because the low E-field issue has been shown. It can be observed from the figure that,

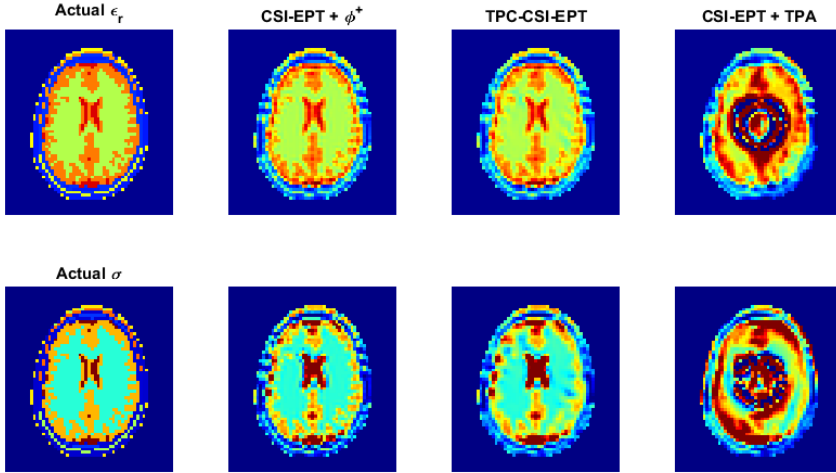


Figure 4.13: Reconstruction by regular CSI-EPT with pure ϕ^+ input, Transmit Phase Correcting CSI-EPT under channel-wise Tx and quadrature Rx mode, and regular CSI-EPT implementing TPA based on a head model. Resolution is 20×20 mm. Iteration number is 200. Array radius is 15 cm.

after 200 iterations, Transmit Phase Correcting CSI-EPT reaches a result that is as good as regular CSI-EPT with perfect input (pure transmit phase), where the boundaries are reconstructed equally well; while regular CSI-EPT with TPA input corrupts severely, due to expected asymmetry problem and low E-field issue.

4.4. SUMMARY

After discussions of this chapter, we have got some knowledge about the field maps, including the formation of the patterns and how are they affected by magnetic field strength, target geometry, transceive elements and electrical properties, through which we verified the non-negligible low E-field issue when implementing a birdcage as transceiver. In addition, we investigated Transceive Phase Assumption, which is the conventional method on handling the absence of transmit phase and should perform relatively well for birdcage mode [3]. After which we draw the conclusion that, TPA is not sufficient for EPT in application. Moreover, we presented our new method, Transmit Phase Correcting CSI-EPT, which iteratively corrects the input transceive phase data towards pure transmit phase. And this improved CSI-EPT algorithm leads to high-quality reconstructions based on a homogeneous cylindrical object, and a proper reconstruction based on a 2D synthetic head model within 200 iterations. However, with the head model, regular CSI-EPT with transmit phase input can reach an almost perfect reconstruction after 500 iterations, with very sharp details; while the reconstruction of Transmit Phase Correcting CSI-EPT starts diverging after 200 iterations. About this divergence, we have two hypotheses: 1) the optimizing direction of Transmit Phase Correcting CSI-EPT is not optimal, since the change of cost function leads to changes on function gradient, which is

Descriptions	Regular CSI-EPT	Regular CSI-EPT + TPA	Transmit Phase Correcting CSI-EPT
Channel-wise TxRx	Prototype, impractical	Not valid from principle	Unstable
Channel-wise Tx, quadrature Rx	Same as above	Not valid from principle	Proper reconstruction, practical
Quadrature TxRx	Low E-field issue, impractical	Low E-field issue, circularity-loss-induced corruption	Low E-field issue

Figure 4.14: Summarized evaluation of different CSI-EPT algorithms and implementations.

not changed in our case, or 2) due to the error accumulation during updating.

Fig. 4.14 summarizes the descriptions of different CSI-EPT algorithms and implementations according to discussions of this chapter.

REFERENCES

- [1] M. Vaidya *et al.*, *Dependence of B_1^+ and B_1^- field patterns of surface coils on the electrical properties of the sample and the MR operating frequency*, *Concepts in Magnetic Resonance Part B: Magnetic Resonance Engineering* **46**, 25 (2016).
- [2] C. Collins *et al.*, *Different excitation and reception distributions with a single-loop transmit-receive surface coil near a head-sized spherical phantom at 300 MHz*, *Magnetic Resonance in Medicine* **47**, 1026 (2002).
- [3] A. vanLier *et al.*, *Electrical properties tomography in the human brain at 1.5, 3, and 7T: A comparison study*, *Magnetic Resonance in Medicine* **71**, 354 (2013).
- [4] H. Wen, *Noninvasive quantitative mapping of conductivity and dielectric distributions using rf wave propagation effects in high-field MRI*, *Proc. SPIE* **471-477**, 5030 (2003).

5

EXPERIMENTAL STUDIES

This chapter investigates the experimental feasibility of CSI-EPT using a transceive array.

The previous chapter studied CSI-EPT through simulations, after which we came to the following conclusions:

- To implement CSI-EPT in practice, birdcage is not suggested due to low E-field issue;
- Transceive Phase Assumption cannot be satisfied in clinical conditions;
- Transmit Phase Correcting CSI-EPT has a good performance on correcting the input transceive phase towards transmit phase, but there's still improvements needed on the optimizing direction;
- Channel-wise transmission quadrature reception is a sufficient transceive mode, which has the potential for other methods to retrieve transmit phase from transceive phase.

In this chapter, we study from the scanned data of a cylindrical phantom, in terms of their correspondence to simulation reference and their performance in CSI-EPT reconstruction. The experiment setup has been introduced in the third chapter. This chapter will discuss about the mismatch between scanned data and simulations first, by describing the mismatch, locating the error source and managing to improve the correspondence as possible. Afterwards, the improved measured B_1^+ data will be evaluated further in terms of the corresponding CSI-EPT reconstruction.

5.1. MEASURED TRANSMIT FIELD DATA EVALUATION

We acquired the transmit field on a cylindrical phantom, with channel-wise RF signal transmission and quadrature reception using a four-channel dipole array. More information about the coil, phantom and sequence have been introduced in the third chapter. The measured data is shown in fig. 5.1. To evaluate the measured data, we take the synthetic RF fields that are simulated in the 2D model as the reference, which is shown in fig. 5.2. By comparing these two groups of images, it can be observed that, there are differences between measured and simulated data, both in terms of phase and amplitude. These differences can arise from many sources: the difference between the estimated incident fields and the actual incident fields; the difference between the synthetic and actual targets' contrast; the deviation between 2D approximation and the 3D configuration, as summarized in the tree graph 5.4. In this section, we will locate the source error and will manage to improve the measured data from two aspects: incident field calibration and 2D approximation. During the investigation, another reference will be included - 3D simulation by XFDTD (Remcom inc., State College, PA, USA).

5.1.1. INCIDENT FIELD CALIBRATION

The incident fields of the four channels are generated by a four-by-four current density matrix. In our 2D simulations, the current density matrix is defined to be the identity matrix with a scaling factor. However, in actual conditions, the incident fields are more complex. For example, the actual incident fields can be affected by: 1) an arbitrary scaling in amplitude, 2) a global phase shift due to cable length in front of the antenna, and 3) transceiver coupling.

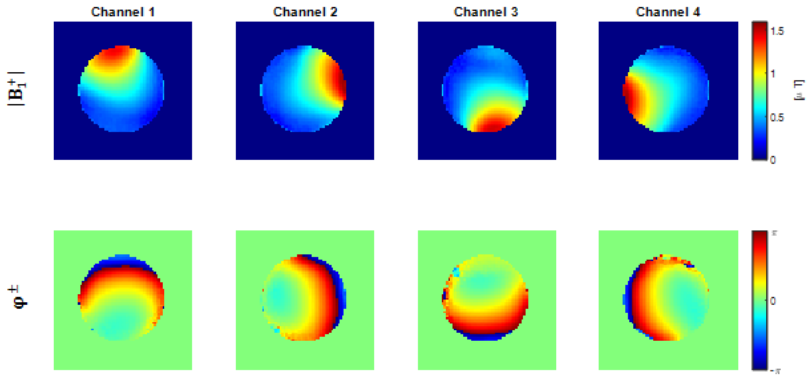


Figure 5.1: Scanned transmit field data.

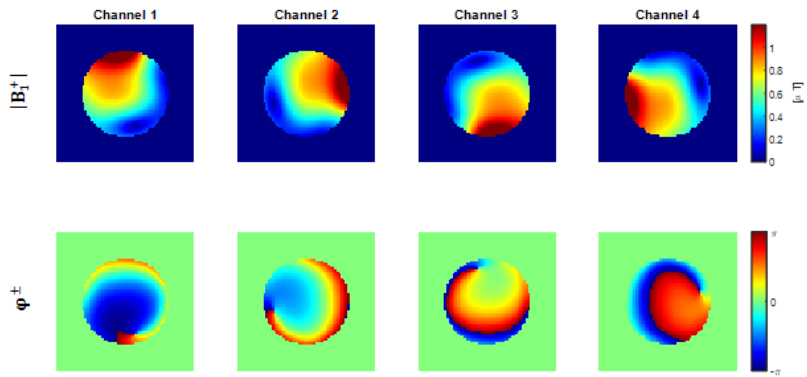


Figure 5.2: Simulated transmit field data from the 2D model.

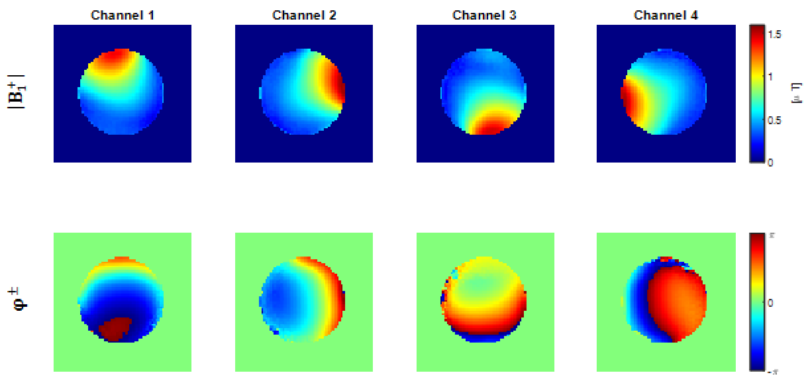


Figure 5.3: Scanned transmit field data after global phase shift correcting.

This part will discuss about the incident field calibration in terms of the above three factors.

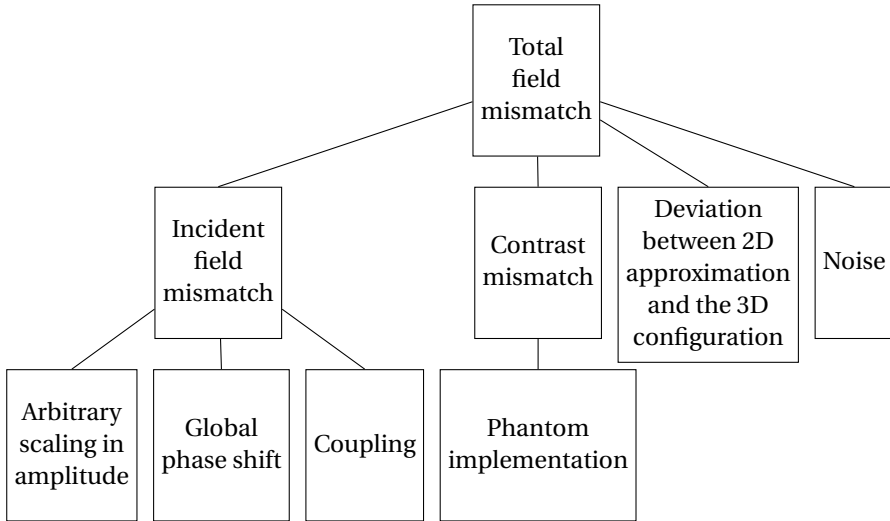


Figure 5.4: Potential error sources of the mismatch between measured and 2D simulated B_1^+ field. The levels from the top to the bottom corresponds to phenomenon to sources.

ARBITRARY SCALING IN AMPLITUDE

As aforementioned, the incident fields are generated by the current density matrix at antenna ports, while the absolute value of the current densities are unknown. As a result, there is a scaling factor between the amplitude of the estimated incident fields and the actual incident fields. In our experiment, since we have the simulation reference, the scaling can be done artificially by minimizing the error between the simulated field and the measured field.

GLOBAL PHASE SHIFT

There is a global phase shift in the transceive phase maps due to cable length in front of the dipoles. In simulation, the starting point of RF wave transmission is modeled at the feed of the dipoles. While in practice, this is at the coil plug. Hence, the wave travels a bit longer before arriving dipole. Therefore, these phase shifts should be quantified by measuring the cable length or through a pre-acquisition, in order to ensure that the phase of signal source in measured data is consistent with that of the estimated incident fields. The measured transmit fields after global phase shift correcting is shown in fig. 5.3, where the transceive phase has a much higher correspondence with 2D simulation than before correcting.

COUPLING ISSUE

In order to identify the relevance of coupling, we removed three dipoles from the array and acquired the transmit field data with a single dipole. The comparison between cou-

pled and decoupled field maps is shown in fig. 5.5. As shown in the figure, when using a single dipole, the amplitude map appears significantly different from that of a four-channel dipole array; while it shows a high similarity to the decoupled 2D simulation.

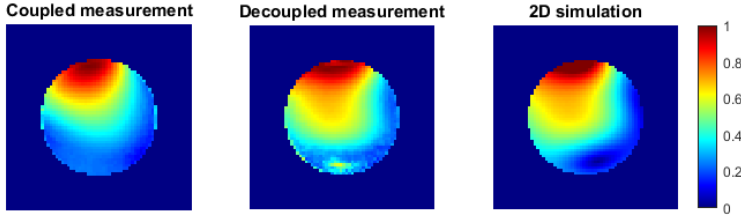


Figure 5.5: Relevance of coupling. Shown are measured B_1^+ data with four-channel dipole array (left), measured B_1^+ data with a single dipole (middle), simulated data via the 2D model (right).

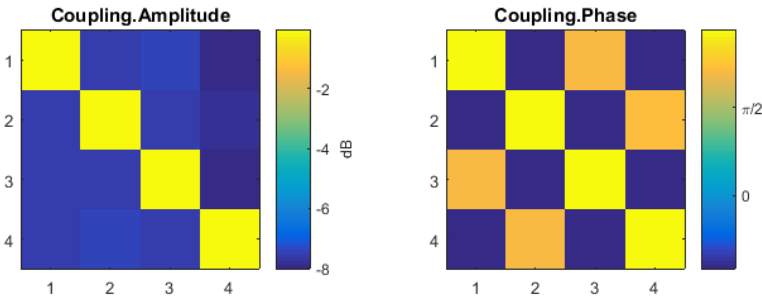


Figure 5.6: Coupling matrix from the 3D simulation.

To avoid this coupling issue, we have two options: 1) decouple the dipoles by hardware improvement, or 2) calibrate the incident fields to incorporate the coupling effect. In this project we implemented the latter option.

The current density matrix which determines the incident fields can be used to incorporate coupling. As aforementioned, the current density matrix is defined to be a scaled identity matrix in our 2D simulation, which means coupling-free. To obtain the coupling matrix (current density matrix), we built a 3D model of the setup, using XFDTD, where the currents on circuit components can be read out directly, as well as the current matrix at the ports of four channels. Due to the linear relation between current matrix, current density matrix and coupling matrix, the current matrix from 3D model should be able to characterize the coupling condition.

Fig. 5.6 shows the coupling matrix obtained from the 3D simulation, fig. 5.7 presents measured data from the four-channel dipole array which includes coupling, the center-slice of a 3D simulation via XFDTD and the 2D simulation with a calibrated incident field that is coupled via the 3D simulation. By comparing fig. 5.5 and fig. 5.7, we can see

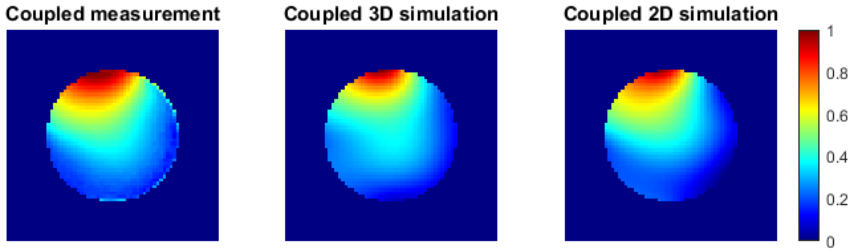


Figure 5.7: Performance of incident field coupling. Shown are measured data (left), center slice of 3D simulation via XFDTD (middle), coupled 2D simulation (right). All fields are normalized to their maximum.

that, the correspondence between 2D simulation and measurement has improved significantly after implementing the coupling matrix from the 3D model.

Besides, in practice, the object would be unknown, so the coupling of incident fields cannot be done by 3D modeling of actual conditions, but the coupling matrix can be derived from the scattering matrix of channels, which is available from acquisitions. However, if a matching circuit is incorporated between dipole ports and RF signal generator, the readout scattering matrix and the coupling matrix at dipole ports would be in different domains, then a junction scattering matrix would be required for the transformation between two domains.

5.1.2. 2D APPROXIMATION

As shown in the last part, after incorporating coupling into the incident fields, the simulated transmit fields based on the 2D model achieved a much better correspondence to the measured fields, but there is still a small deviation that can be observed visually. One remaining error source is 2D approximation.

As aforementioned, a 2D model comes from the assumption of $\partial_z = 0$, which means no variance of its expansion along the third dimension under Transverse Magnetic (TM) waveguide mode, mathematically say, $\{E_x, E_y, B_z\} = 0, \{B_x, B_y, E_z\} \neq 0$. In order to test this approximation, we compare the transmit field of the center slice of 3D simulation with our 2D simulation, both with a single dipole as transceiver to keep the configuration simple and to avoid interference from other variables as possible. The comparison between 2D and 3D transmit field maps is shown in fig. 5.8, where an obvious mismatch can be recognized visually. As presented in the third chapter, the dipole we are using for experiments has only one source at the center, which means, there has to be a decay of currents along z-direction, from the source to the end of the dipole. Therefore, for further evidence, another enhanced version of 3D model was also simulated - where a 20 cm long dipole is composed of series connected feeds with consistent current distribution. The enhanced model is simply the expansion of 2D point source along the third direction, therefore it should lead to a better 2D approximation in principle. The simulated transmit field of this single all-feed dipole is shown in fig. 5.9, where the center region is improved dramatically towards the 2D model. Therefore, according to the field

maps, it seems like a transceiver with less current variance along z-direction is closer to a 2D model, which means, the 2D approximation is not always sufficient to model the 3D configurations. The next section will make further evaluation from the CSI-EPT reconstruction aspect.

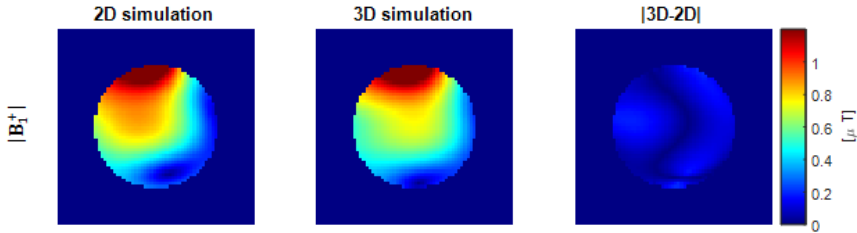


Figure 5.8: Correspondence between actual dipole and 2D approximation. Shown are decoupled 2D simulation (left), decoupled 3D simulation based on the 3D model of the actual dipole (middle), the difference between them (right).

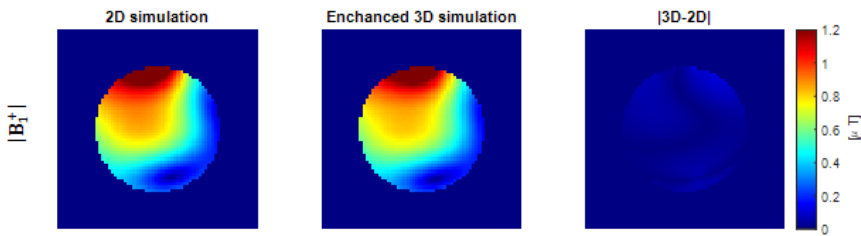


Figure 5.9: All-feed dipole. Dipole length = 20 cm.

5.2. CSI-EPT WITH MEASURED TRANSMIT FIELD INPUT

For further evaluation, we also input the measured data to Transmit Phase Correcting CSI-EPT reconstruction. Fig. 5.10 shows the reconstruction with the measured field data before incident field calibration as the input. Since significant mismatch from expectation has been observed on measured data, it is not a surprise to observe corruption in the reconstructed results. The reconstruction is saturated after 100 iterations, however the reconstructed result does not correspond well to the known electrical properties of the phantom. Fig. 5.11 shows the CSI-EPT reconstruction after incident field calibration, where we can see the reconstructed result is slightly improved in the centered region compared to that before incident field calibration, despite significant improvement in transmit fields after incident field calibration. There is still strong deviation between actual and reconstructed electrical properties, which is probably the 2D approximation loss.

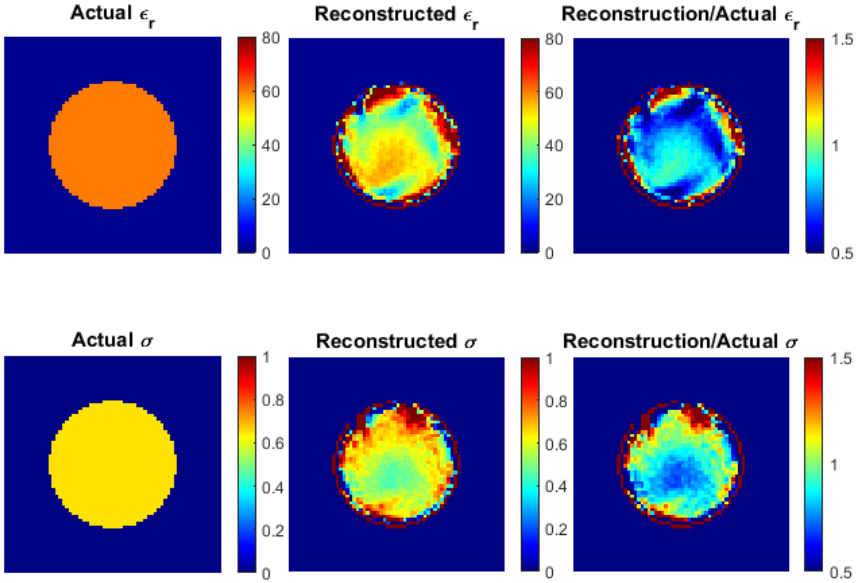


Figure 5.10: Transmit Phase Correcting CSI-EPT reconstruction based on measured data, after 200 iterations.

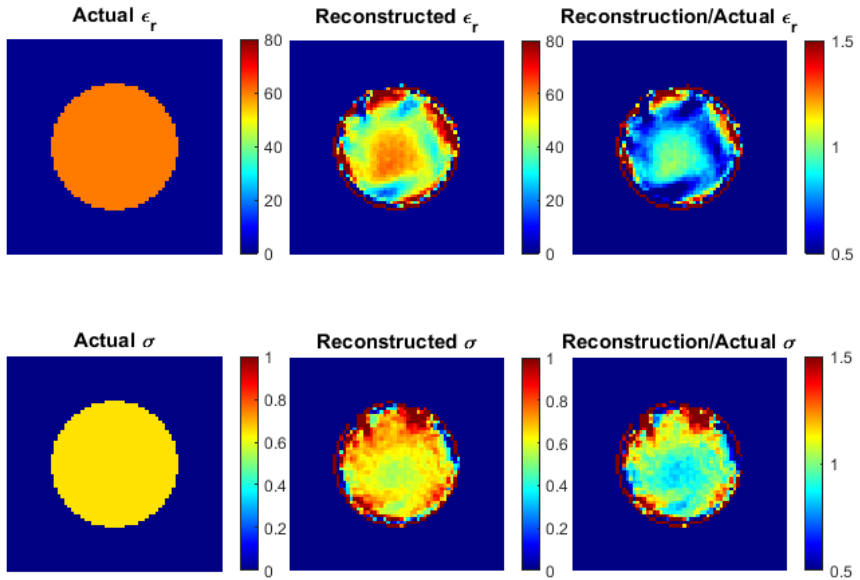


Figure 5.11: Transmit Phase Correcting CSI-EPT reconstruction based on measured data with a calibrated incident field, after 200 iterations.

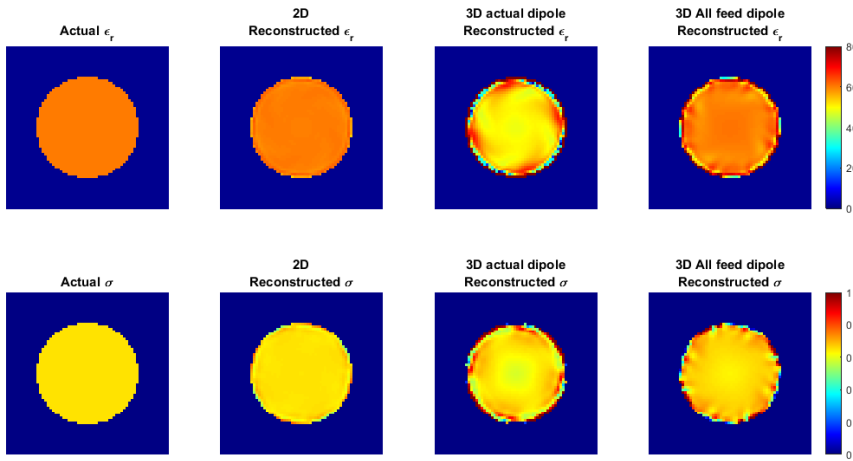


Figure 5.12: Transmit Phase Correcting CSI-EPT reconstructions based on simulations from the 2D model, 3D model which mimics the practical condition, 3D model with a 30cm all-feed dipole. Iteration number = 200.

To confirm the 2D approximation effect from the reconstruction side, three groups of 2D and 3D simulated transmit fields were fed into Transmit Phase Correcting CSI-EPT reconstruction, which are simulated transmit fields respectively based on the 2D model, the 3D model with the actual dipole, the enhanced 3D model with the 20 cm all-feed dipole. For simplicity, a decoupled scenario was evaluated. The reconstructed results are shown in fig. 5.12.

As shown in fig. 5.12, synthetic data from 2D model achieves a high-quality reconstruction, but 3D case with the actual dipole does not. Moreover, we can even recognize some correspondence between 3D-simulation-leading and measurement-leading reconstructions by comparing fig. 5.12 and fig. 5.11, for instance the general underestimation of permittivity and the ring-shape overestimation of conductivity. Which means, the mismatch between 2D approximation and the 3D configuration is probably relevant to the corruptions of the measurement-leading reconstruction. Furthermore, the enhanced 3D model shows a significant improvement in reconstructed results comparing to the actual 3D model. The improvement of the enhanced 3D model is even more convincing to show that the variance along z-direction deteriorate the correspondence between the 3D model and the corresponding 2D approximation.

5.3. SUMMARY

In this chapter, we evaluated the experimental feasibility of 2D CSI-EPT using a transceive array. We assessed the measured data with the reference of 2D and 3D simulations, where we located the source of transmit field mismatch:

- The incident field mismatch due to arbitrary scaling, global phase shift and coupling between dipoles;
- The mismatch between 3D configuration and the 2D approximation.

About the calibration of incident fields, the global phase shift can be done by measuring the cable length; the coupling matrix can be obtained from the scattering matrix from acquisition; while the calibration of the arbitrary scaling still needs further study.

The insufficiency of 2D approximation is proved to be arise from the variance along z -direction. To get rid of the 2D3D gap, either a dipole with homogeneous current distribution along z -axis is designed, or we have to move on to 3D CSI-EPT study. Moreover, even if a dipole with homogeneous current distribution is successfully designed, the variance of the object along z -direction needs to be considered.

6

CONCLUSION

In this thesis, we have assessed the feasibility of CSI-EPT both through simulations and phantom experiments, with different implementations of parallel transceive elements.

In simulation studies, we implemented a 2D model, which approximates the actual conditions by assuming longitudinal variance. Through these simulations upon the 2D model, we have described the effects of the magnetic field strength, electrical conductivity, object geometry to radiofrequency field; we have evaluated the Transceive Phase Assumption (TPA), which is the conventional method to deal with the unavailability of transmit phase in EPT. Moreover, we have introduced a new method to adapt regular CSI-EPT to transceive phase inputs: Transmit Phase Correcting CSI-EPT, where we reformulate the data as the transmit amplitude with transceive phase, or equivalently, we reconstruct the transmit field with transceive phase. The evaluation of the above algorithms have been performed with respect to different implementations of a four-channel dipole array: channel-wise mode and quadrature mode, and the evaluated result is summarized in fig. 4.14. Through simulation studies, we have drawn the following conclusions:

For handling the unavailability of exact transmit phase,

- TPA is not sufficient, due to the loss of circularity of the field polarization, resulting from the interference from object-induced currents and scattering;
- Transmit Phase Correcting CSI-EPT is capable of proper reconstructions in terms of both homogeneous cylindrical phantom and a 2D synthetic head model.

For transceive elements,

- implementing quadrature mode (birdcage mode) both for transmission and reception will lead to low E-field issue;
- implementing channel-wise transmission and quadrature reception can avoid low E-field issue and leads to stable Transmit Phase Correcting CSI-EPT reconstructions.

In experimental studies, we acquired transmit field data with DREAM, a fast B_1 acquisition method. We have refined the measured data in the following steps:

- Compensating the eddy current effect by conducting another scan with reversed readout gradient polarity;
- Calibrating the incident field in terms of the global phase shift, coupling between dipoles, and arbitrary scaling.

Furthermore, we have proved that there exists discrepancy between the 2D approximation and the 3D configuration, which deteriorates the performance of CSI-EPT. This is proved by comparing the transmit fields generated upon the 3D model to those from the 2D approximation. Moreover, we have also proved that, the discrepancy can be improved by improving the uniformity of the currents along the longitudinal direction.

After this project, a few follow-up research topics are suggested below:

- About the incident field calibration, the aforementioned arbitrary scaling factor in amplitude of the incident fields is load-impedance-dependent. As a result, it cannot be characterized by a pre-scan or by simulation when the object is unknown. Therefore, incident field calibration with respect to this scaling factor should be figured out before practical implementation of CSI-EPT.
- Transmit Phase Correcting CSI-EPT shows divergence during updating, the source of which has to be located before practical implementation. Where we have two hypothesis: optimizing direction may need to be changed due to the change of cost function, where a new variable about the contrast source has been included; it may be the error accumulation after iterations, which results in divergence.
- When implementing the transceive mode channel-wise transmission and quadrature reception, the transmit phase should be calculatable as: the quadrature combination of measured data of four channels should be equivalent to $Nel+1$ times receive phase, where Nel is the number of channels. And, these four channels have a common receive phase. Therefore, the transceive phase is measured, and the receive phase is able to be calculated from measured data, then the transmit phase can be calculated.
- We have proved that the deviation between 2D approximation and the 3D model results from the variation of E-field along z-direction. Therefore, if one wants to apply 2D CSI-EPT to measured data, the transceiver has to be able to drive currents uniformly along z-direction. Moreover, the effect of variation of object's electrical properties along z-direction to the accuracy of 2D approximation also needs to be investigated.

This is the end of this thesis. We hope our research contributes to the development of CSI-EPT, towards clinical implementation.

A

POLARIZATION OF RF FIELDS

In the chapter Simulation Studies, we have shown the different polarization modes of transmit fields when implementing different transceive modes, in forms of field maps. In this part, we will explain the polarization modes under different transceive modes from mathematical aspects, with no object.

Recall the transmit field equations:

$$B_1^+ = \frac{B_{1x} + jB_{1y}}{2}, \quad (\text{A.1a})$$

$$B_1^- = \frac{B_{1x} - jB_{1y}}{2}, \quad (\text{A.1b})$$

where B_{1x} and B_{1y} are x-component and y-component of B_1 field. The x,y-components can be represented with the following equations:

$$B_{1x} = KI_o C_x e^{j(\phi+\alpha)}, \quad (\text{A.2a})$$

$$B_{1y} = KI_o C_y e^{j(\phi+\beta)}, \quad (\text{A.2b})$$

Combining eq. A.1 and eq. A.2, we have

$$B_1^\pm = \frac{B_{1x} \pm jB_{1y}}{2}, \quad (\text{A.3a})$$

$$= \frac{KI_o}{2} (C_x e^{j(\phi+\alpha)} \pm jC_y e^{j(\phi+\beta)}). \quad (\text{A.3b})$$

Then apply Euler's formula ($e^{jx} = \cos(x) + j \sin(x)$) to the above equation, we come to

$$|B_1^\pm| = \frac{KI_o}{2} \sqrt{C_x^2 + C_y^2 \mp 2C_x C_y \sin(\beta - \alpha)}, \quad (\text{A.4a})$$

$$\phi^+ = \arctan \frac{C_x \sin(\phi + \alpha) + C_y \cos(\phi + \beta)}{C_x \cos(\phi + \alpha) - C_y \sin(\phi + \beta)}, \quad (\text{A.4b})$$

$$\phi^- = \arctan \frac{C_x \sin(\phi + \alpha) - C_y \cos(\phi + \beta)}{C_x \cos(\phi + \alpha) + C_y \sin(\phi + \beta)}. \quad (\text{A.4c})$$

LINEAR POLARIZATION IMPLEMENTING A SINGLE DIPOLE

In linearly polarized fields, $\alpha = \beta$, then the above equations A.4 become

$$|B_1^+| = |B_1^-| = \frac{K I_0}{2} \sqrt{C_x^2 + C_y^2}, \quad (\text{A.5a})$$

$$\phi^+ = \arctan \frac{C_x \sin(\phi \pm \alpha) + C_y \cos(\phi + \alpha)}{C_x \cos(\phi + \alpha) \mp C_y \sin(\phi + \alpha)} = \phi + \alpha \pm \arctan \frac{C_y}{C_x}, \quad (\text{A.5b})$$

$$\phi^- = \arctan \frac{C_x \sin(\phi + \alpha) \mp C_y \cos(\phi + \alpha)}{C_x \cos(\phi + \alpha) \pm C_y \sin(\phi + \alpha)} = \phi + \alpha \mp \arctan \frac{C_y}{C_x}, \quad (\text{A.5c})$$

$$\frac{\phi^+ - \phi^-}{2} = \phi^+ - (\phi + \alpha), \quad (\text{A.5d})$$

where the upper and the lower symbols are respectively for an even k and an odd k . When $\phi + \alpha = 0$, we have $\frac{\phi^+ - \phi^-}{2} = \phi^+$. ϕ is the phase of input current, so when there is only one dipole, ϕ has no spatial variance. α is the phase delay between the dipole and the measured point, and it has lower spatial variance when the wavelength is longer, which is equivalent to the higher static magnetic field strength or a lower background permittivity. For example, when B_0 is under 0.5 T, the spatial variance of α is negligible, as shown in fig. A.1. Therefore, when implementing a single dipole at low magnetic field, we have

$$\lim_{\alpha \rightarrow 0} \frac{\phi^+ - \phi^-}{2} = \phi^+ - \phi, \quad (\text{A.6})$$

$$\lim_{\alpha \rightarrow 0} \frac{\phi^+ + \phi^-}{2} = 2\phi, \quad (\text{A.7})$$

where ϕ is a constant scalar, which is usually 0 or predictable, the corresponding visualization is shown in fig. A.2. Eq. A.7 proves that Transceive Phase Assumption is not valid when the field is linearly polarized.

As magnetic fields strength or the background permittivity ϵ_r increases, the wave number increases, resulting in more spatial variance of α , as shown in fig. A.3, which further leads to the rotating pattern of incident field maps at high-field, as shown in fig. A.4.

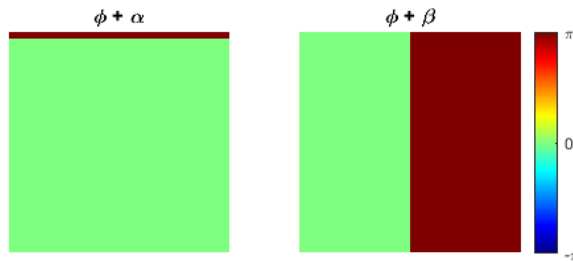


Figure A.1: Phase maps of B_{1x} and B_{1y} at 0.5 T with a single dipole.

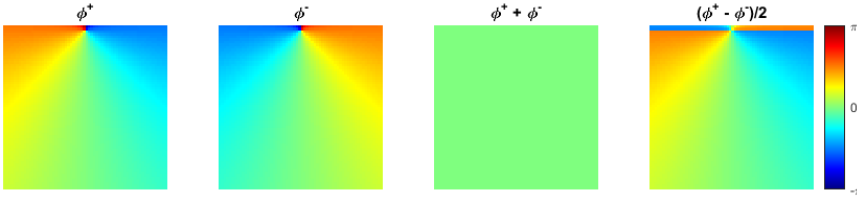


Figure A.2: Transceive phase maps at 0.5 T with a single dipole.

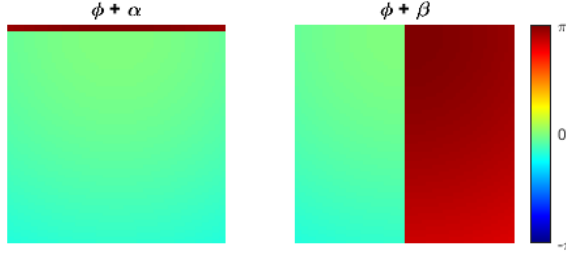


Figure A.3: Phase maps of B_{1x} and B_{1y} at 7T with a single dipole.

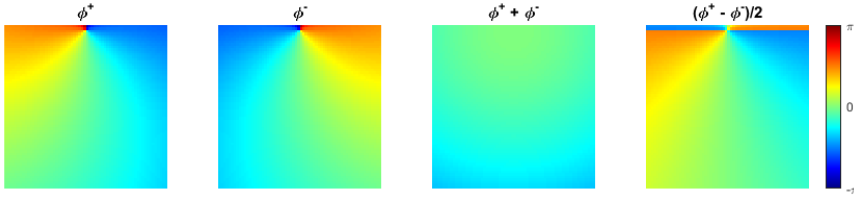


Figure A.4: Transceive phase maps at 7T with a single dipole.

CIRCULAR POLARIZATION IMPLEMENTING CP1

When implementing CP1+ transceive mode with a four-channel dipole array, the relation between the x- and y- component of RF fields can be written as $\alpha = \beta + (\frac{\pi}{2} + \theta)$, $C_x = C_y$, where θ is a spatial dependent phase term, as presented in the third column fig. A.6. Then eq. A.4 becomes

$$|B_1^+| = |B_1^-| = \frac{KI_0}{2} |C_x + C_y|, \quad (\text{A.8a})$$

$$\phi^+ = \arctan \frac{C_x \sin(\phi + \alpha) + C_y \sin(\phi + \alpha - \theta)}{C_x \cos(\phi + \alpha) + C_y \cos(\phi + \alpha - \theta)}, \quad (\text{A.8b})$$

$$\phi^- = \arctan \frac{C_x \sin(\phi + \alpha) - C_y \sin(\phi + \alpha - \theta)}{C_x \cos(\phi + \alpha) - C_y \cos(\phi + \alpha - \theta)}, \quad (\text{A.8c})$$

$$(\text{A.8d})$$

corresponding to fig. A.5 and A.6. When it goes to the center of the transceive fields, the field polarization goes circular, θ goes to 0, then we have

$$\lim_{\theta \rightarrow 0} \phi^+ = \phi + \alpha, \quad (\text{A.9})$$

which corresponds to the homogeneous transmit phase map when using CP+ excitation. Besides,

$$\lim_{\phi + \alpha \rightarrow 0} \phi^- = \frac{\sin \theta}{1 - \cos \theta}, \quad (\text{A.10})$$

which corresponds to the radial patterns of receive fields under CP1+ mode, as shown in fig. A.7.

When implementing CP1- excitation mode, the relation becomes $\alpha = \beta - (\frac{\pi}{2} + \theta)$, then eq. A.4 becomes

$$|B_1^+| = |B_1^-| = \frac{KI_0}{2} |C_x - C_y|, \quad (\text{A.11a})$$

$$\phi^+ = \arctan \frac{C_x \sin(\phi + \alpha) - C_y \sin(\phi + \alpha + \theta)}{C_x \cos(\phi + \alpha) - C_y \cos(\phi + \alpha + \theta)}, \quad (\text{A.11b})$$

$$\phi^- = \arctan \frac{C_x \sin(\phi + \alpha) + C_y \sin(\phi + \alpha + \theta)}{C_x \cos(\phi + \alpha) + C_y \cos(\phi + \alpha + \theta)}, \quad (\text{A.11c})$$

$$(\text{A.11d})$$

Also,

$$\lim_{\theta \rightarrow 0} \phi^- = \phi + \alpha, \quad (\text{A.11e})$$

$$\lim_{\phi + \alpha \rightarrow 0} \phi^- = \frac{-\sin \theta}{1 - \cos \theta}, \quad (\text{A.11f})$$

Therefore, the transmit phase of CP+ corresponds to receive phase of CP-, both with a homogeneous distribution; the receive phase of CP+ is the opposite of the transmit phase of CP-, both appear radial. Furthermore, the correspondence is consistent as the static magnetic field strength or the background magnetic field increases, which only increases the spatial variance of α .

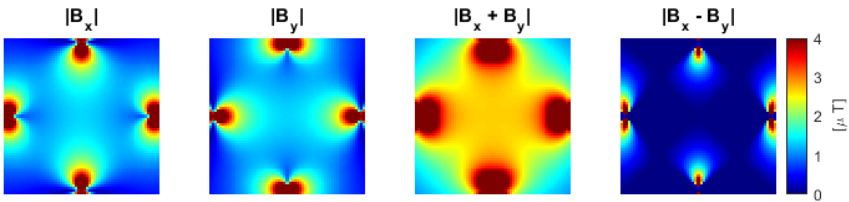


Figure A.5: Amplitude maps of B_{1x} and B_{1y} at 0.5 T under CP1 mode.

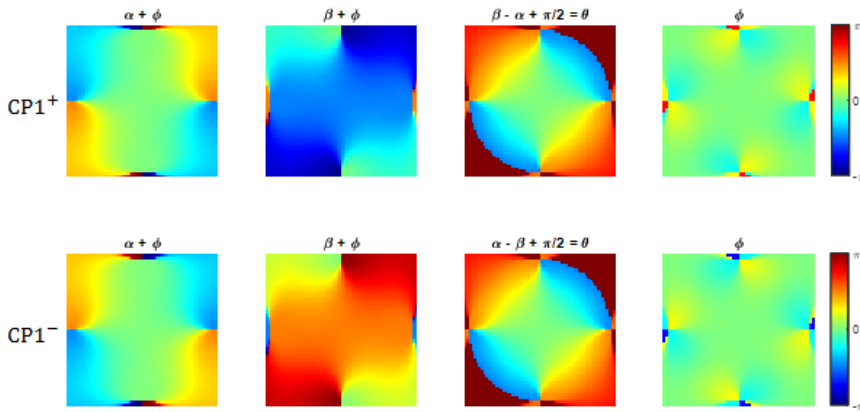


Figure A.6: Phase maps of B_{1x} and B_{1y} at 0.5 T under CP1 mode.

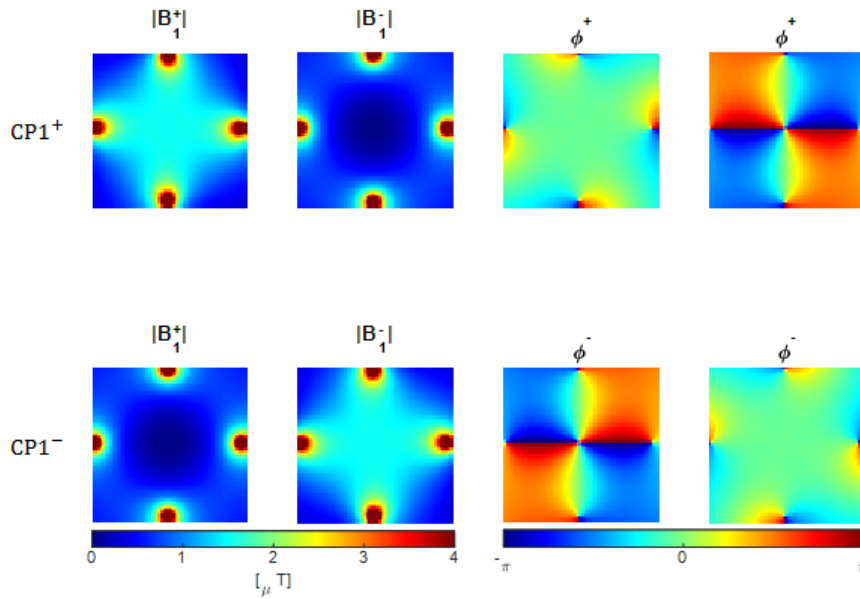


Figure A.7: Transceive field maps at 0.5 T under CP1 mode.

ACKNOWLEDGEMENTS

First and foremost, I have to thank my research supervisor Dr. ir. R.F. Remis and Dr. ir. W.M. Brink for giving me the opportunity to have a valuable research experience. Also thank Dr. Brink for his patience, motivation and guidance. I would also like to show gratitude to my committee, including Dr. R.F. Remis, Dr. M. Spirito, Dr. C.A.T. van den Berg. Furthermore, I would like to thank my colleagues at the C.J. Gorter Center for being great examples. I have enjoyed the company of my friends in LUMC, Andrea, Wico and Koen. I thank Reijer for his generous help during this project. I thank my honest friend Fanyu for her encouragement. Most importantly, I am grateful to my parents for their unconditionally support.